國立交通大學

機械工程學系

博士論文

抓爬式靜電微致動器之模擬及低電壓區輸出特性的改善

Modeling of Scratch Drive Actuator and Performance Enhancement in Low-Voltage Region

研 究 生: 陳 雄 章

指導教授: 徐 文 祥 博士

中華民國九十九年七月

抓爬式靜電微致動器之模擬及
低電壓區輸出特性的改善

Modeling of Scratch Drive Actuator and Performance Enhancement in Low-Voltage Region

研 究 生：陳雄章　　Student: Shawn Chen

指導教授：徐文祥　　Advisor: Wensyang Hsu

國 立 交 通 大 學

機 械 工 程 學 系

博 士 論 文

A Dissertation
Submitted to Department of Mechanical Engineering
College of Engineering
National Chiao Tung University
in partial Fulfillment of the Requirements
for the Degree of PhD
in

Mechanical Engineering

July 2010

Hsinchu, Taiwan

Modeling of Scratch Drive Actuator and Performance Enhancement in Low-Voltage Region

Student：Shawn Chen　　Advisor：Wensyang Hsu

Department of Mechanical Engineering
National Chiao Tung University

Abstract

An improved model is proposed to reduce the cost due to trial and error in selection of Scratch Drive Actuator (SDA) geometry, driving voltage and output force level. Besides, a novel SDA design to reduce driving voltage from at least 80 volts to 40 volts to get better reliability with comparable output is also proposed. It is assumed that the deformation and property of SDA is same along the width direction, as the main plate may be treated by a beam model. Governing equation based on Euler-Bernoulli beam is first constructed. Solving this equation with proper boundary conditions, key SDA characteristics can be determined analytically, such as non-contact length, priming voltage, deflection curve, output force, bending moment and stress. The output force just stated is the input of SDA dynamic model of single degree-of-freedom including friction. To verify proposed model, electroplated nickel SDA arrays of 80 μm in length and 65 μm in width with suspended spring are fabricated and tested. The average travel distance after 1500 input pulses from 80 to 120 volts are measured to be from 5.9 to 13.9 μm, while average measured output forces are from 12.4 to 30.2 μN per SDA. Deviations between simulated and measured results are less than 10%, showing the superior ability of the proposed integrated SDA model for better performance prediction.

A low-voltage scratch drive actuator (LVSDA) is also proposed here by incorporating flexible joint into the conventional rectangular SDA to improve performance in low-voltage region. Experimental results show that, at the same total plate length of 80 μm and width of 65 μm, the proposed LVSDA can be actuated as low as 40 volts, much lower than 80 volts, the minimum required input voltage of conventional SDA. From nonlinear finite element analysis conducted by CosmosWorks, yielding effect is found to be a critical factor. Before yielding, LVSDA can provide better performance than SDA at the same input voltage. However, the yielding stress in flexible joint would limit the achievable maximum output force in high-voltage region. By varying joint length, width, or location, LVSDA has been operated in low-voltage region where the conventional SDA can not be operated, and can still provide comparable performance as SDA in high-voltage region. The proposed LVSDA design can provide more flexibility in design selection to meet different performance requirements.

抓爬式靜電微致動器之模擬及低電壓區輸出特性的改善

學生：陳雄章　　指導教授：徐文祥

國立交通大學機械工程學系

摘　要

抓爬式靜電微致動器(SDA)有微牛頓等級輸出力、在數十奈米等級步進尺寸下可行進達數毫米。迄今，此類致動器的幾何尺寸選擇主要依賴經驗，驅動電壓及輸出力亦需經由實驗測試後方有依據。為減少試誤法造成成本負擔，發展系統化的解析模型有其必要性。此外傳統矩形抓爬式微致動器的啟動電壓常超過 80 伏特，容易造成介電層崩潰之可靠度問題。因此開發新設計以降低操作電壓、能源消耗、並維持足夠輸出力及可靠度是另一研究重點。

本研究第一部份旨在建立抓爬式微致動器的較符合現實情況之解析模型，並以面型鎳基微加工技術製作。由於抓爬式微致動器的運動以單一方向為主，假設其沿寬度方向的變形及應力分佈一致；因此可依據 Euler-Bernoulli 樑的模型，配合適當的邊界條件以解出相關的積分常數，再依序推導如未接觸長度、貼底(priming)電壓、變形曲線、輸出力、彎矩及最大正向應力等特徵。上述輸出力可設為單自由度運動方程式的輸入。在長 80 微米、寬 65 微米的尺寸下，以 80 到 120 伏特為輸入範圍，其步進尺寸預測值在 22 到 41 奈米之間。以 500Hz 電壓測試結果發現，1500 次輸入脈波所得總行程位移介於 5.9 到 13.9 微米；每個抓爬式微致動器輸出力介於 12.4 到 30.2 微牛頓，其測試結果與預測值誤差小於 10%，顯示本文提出之解析模型具有可預測輸出力的較佳實用性。

本研究第二部份提出一種新式可在較低電壓驅動的抓爬式微致動器設計，主要是將撓性接頭加入傳統矩形板的中間適當處。在同樣總長 80 微米和寬 65 微米的尺寸下，製作並測試具有不同撓性接頭尺寸及位置的設計，其結果發現啟動電壓最小可降低到約 40 伏，遠低於傳統同尺寸抓爬式微致動器所需要的 80 伏特。當輸入電壓在 40 到 120 伏之間時，其步進尺寸預測值在 9 到 67 奈米之間，而實測輸出力在 4.9 到 19.6 微牛頓之間。證實所提出的新設計可在傳統抓爬式微致動器無法操作的低電壓區有效操作。但有限元素法分析結果亦顯示，在高電壓區的最大輸出力，會受到撓性接頭最大應力達到降伏應力的限制。在此提出的融合撓性接頭的設計，將可提供抓爬式微致動器更大的設計空間，以滿足不同輸出特性的要求。

誌　　謝

謝天謝地謝謝你， 感謝關心與督促。

特別感謝指導教授徐文祥博士。他的美式風格如當頭棒喝讓我頓悟覺醒，終能修成正果，體會作研究的精義、寫論文的方法及待人處世之道。佩服、值得。

感謝交大老師們的無私教誨及傾囊相授，讓我見識理解到教學和研究的典範。

感謝中央大學王國雄教授。在我就讀中大碩士班的指導與提攜，讓我了解學術殿堂的訣竅與奧妙。在交大博士班修業期間，也常鼓勵並提醒相關研究的重點；使我能在關鍵時刻做出恰當的判斷。

感謝各位口試委員教授們的肯定及愷切指導；讓我能將論文修正到更為嚴謹週延。且在研究的未來方向確認出較佳的切入點。

謝謝同門師兄弟的切磋及協助，終於完成博士班的研究訓練。

最要感謝家維學弟在製程及測試的努力與投入，這是我們共同分享的榮耀，Hokila!

感謝內人妙芳的愛與全力支持、父母的養育教導，家人的體貼包容讓我安心完成學業。我愛你們。

終於、 我畢業了。山又是山、水又是水；肩頭上多的是 責任，心裡多的是 理想。如何在各項拘束之間取得平衡，這是一個 重要的課題！

風城的各位，有空到文化城台中說新敘舊、煮酒泡茶、點子就誕生了。再會。

雄章 于 新竹交通大學

2010.07.13

CONTENTS

Figure List

Table List

Notation

V_{pi}	Pull-in voltage
V_{pr}	Priming voltage
V_{pp}	Post-priming voltage
Z_b, Z_n	Bushing height and thickness of dielectric layer, respectively
Z_m	Constant equal to $Z_b + Z_n$
q	Distributed load
e_0	Permittivity of air;
k, k_1	Relative dielectric constant
V	Input voltage
W	Plate width
d	Gap distance between two plates
y	Main beam deflection
Dx	Step size
l	SDA plate length
h	Bushing height
U_d	Elastic energy of bending
U_s	Electrostatic energy of capacitor
U_T	Total energy
l'	Contact length of plate with dielectrics
L''	Plate length
L'	Measured contact length of plate
$x_b(L')$	Bushing position at L'
a	Thickness t of the dielectric layer divided by the relative permittivity k
b	Equal to h / l_n^2
l_n	Non-contact length of main beam at the given input voltage
E	Young's modulus of SDA material
I	Second area moment of main beam
x	Horizontal coordinate of the element in consideration
c_1, c_2, c_3, c_4	Integration constants
k_t	Torsional spring constant of support beam
b	Aspect ratio constant based on ratio of width to thickness of support beam
W_p	Width of support beam
L_p	Length of support beam
G	Shear modulus of SDA material
M	Bending moment at position x in non-contact part of main beam
M_{max}	Maximum moment
x_{max}	Position the maximum moment M_{max} happens along main beam for an input
s_{max}	Maximum bending stress along main beam for an input
F_o	Horizontal output force of charged SDA array
N	SDA number in the SDA array
q	Angle between the horizontal and the tangent line along main beam
Dx_1, Dx_2	Backward displacement of bushing top at pull-in and (post) priming respectively
Dx_{pr}, Dx_{pp}	Step size at priming voltage and post priming voltage, respectively
m	Lump-mass of SDA or LVSDA array including the ring
k	Spring constant of suspended tether spring
c	Viscous damping coefficient between contact surfaces

μ	Coulomb friction coefficient between contact surfaces
F_N	Normal force between contact surfaces
w	Angular velocity of sinusoidal driving voltage
σ_e, σ_y, σ_{ult}	Endurance limit, yielding stress, and ultimate stress, respectively
σ_{max}, σ_{min}	Maximum and minimum bending stress, respectively
s_{av}, s_r	Average and range of bending stress, respectively
s_R	Equivalent fully-reverse stress amplitude of same fatigue life
L_m, L_s	Main plate length and scratch plate length in LVSDA, respectively
L_j, W_j	Length and width of flexible joint in LVSDA, respectively
k_1	Spring constant of one box spring
L_r, W_r	Half length and width of box spring, respectively
F_E	Equivalent electrostatic force
A, B	Characteristic coefficients in Basquin's equation
Dx_0	Step size with zero spring load
$Dx(n)$	Step size at n^{th} input pulse
$x(n)$	Total travel distance after n input pulses

Chapter 1 Introduction

Regular micro actuators can perform nano/micro-meter scale resolution displacement and micro-Newton scale output force. Electrostatic microactuators produce relative high output force per unit input voltage due to their surface-force nature.

1.1 Motivation

Among them, the scratch drive actuator (SDA) is operated mainly in nonlinear manner and in post-priming region. As shown in Figure 1-1 [1], SDA can step forward with 10~100 nm resolution, 1 mm long travel distance and 63 μN output force per SDA at 200V. These good characteristics make the SDA competitive in the field of microactuators. In general, present models of SDA are basically restricted in static region because the complexity from the nonlinear coupling between the electrostatic, mechanical and friction forces. Yet, it is less understood in the MEMS field in spite of its importance. Besides, conventional rectangular SDA is often driven by voltage over 80 volts which is somewhat too high in electronic system.

1.2 Literature review

The scratch drive actuator (SDA) was first proposed by Akiyama and Shono to show the controllable step-wise motion of nano-meter resolution [2, 3]. By transforming the electrostatic energy into mechanical displacement elegantly with friction, SDA is attractive in micro or even nano manipulation. Applications of SDA have been reported in many microelectromechanical systems (MEMS), such as design of platform self-assembly [1,4], optical xyz-stage assembly [5], variable optical attenuator (VOA) assembly by triangular SDA array [6], platform self-assembly by buckled beam [7], microrobot actuation by large SDA array [8], operation of cam-micromotor [9], actuation of micro-fan [10,11], wireless microrobot [12-15],

micro-gripper [16], microtranslation table [17], and inverted SDA array for large area actuation[18]. Some typical devices in these literatures are shown in Figure 1-2. Generally, the required driving voltages in the literatures on are still very high, usually above 80 volts.

In geometrical design of SDA, different shapes on SDA main plate have been reported, and the most common one is the rectangular shape. It was found that the output force was proportional to the width of main plate and square of input voltage [1]. Also, a longer main plate could reduce the minimum required driving voltage, so-called threshold voltage, to activate the SDA [1, 8]. However, the output force of a longer SDA would be smaller than that of a shorter SDA at the same driving voltage in general [1, 8]. Besides the rectangular shape, triangular and trapezoidal shapes [19] also have been reported. In triangular design, the apex is placed at the free edge of main plate. While in trapezoidal design, the wider side is placed at free edge. The yield rates at different dimension-ratio designs were investigated, but output forces at different designs were not mentioned [19]. For the effect on bushing height, it was reported that a bigger step size could be achieved for a larger bushing height with the price of higher input voltage.

Some researches attempted to explore the relation between step size and input voltage of SDA. The step size under constant load is the most fundamental case and has been studied by various methods. One approach was to measure the contact length of charged SDA with insulated layer using interference image, and then calculated the step size from geometry of selected images as in Figure 1-3 [2]. The step size may be calculated from the equation (1-1)

$$\text{Step size } \Delta x = h^2 / 2(l-l') \qquad (1\text{-}1)$$

where l is the SDA plate length, h is bushing height and l' is the contact length of plate by measuring interference image. In [19], an empirical equation (1-2) is used to calculate the step size in Figure 1-4 as following

$$\text{Step size } \Delta x = x_b(L')\text{-}x_b(L'(0)) \tag{1-2}$$

where $L'(0)$ and L' are the measured contact length at beginning $x_b(L'(0)$ and $x_b(L')$, the latter is the bushing position when L'. These two approaches did not relate the step size with input voltage analytically. In [20], the energy method is used to derive and predict the step size and non-contact length of SDA for given input by treating the reaction force at bushing as concentrated load as shown in Figure 1-5. Since electrostatic force did exist along the main beam in SDA operation, the predicted step size was overestimated comparing to measured results. The results in [20] is summarized as following

The Governing equation: $$\frac{d^2y}{dx^2} = -\frac{M}{EI}, \tag{1-3}$$

integrating twice with boundary conditins, then

Deflection curve: $$y = \frac{h}{2l^3}(x^3 - 3l^2x + 2l^3), \tag{1-4}$$

Elastic energy: $$U_d = \frac{EI}{2}\int_0^l [\frac{d^2y}{dx^2}]^2 dx \tag{1-5}$$

Capacitance: $$C = \frac{eW(L-l)}{d}, \tag{1-6}$$

Electrostatic energy: $$U_s = \frac{CV^2}{2}, \tag{1-7}$$

Total energy: $U_T = U_d + U_s$, and when $\frac{dU_T}{dl} = 0$,

Non-contact length: $$l = (\frac{3Edt^3h^2}{4eV^2})^{\frac{1}{4}}, \tag{1-8}$$

and $q \cong \frac{dy}{dx}$ (at $x = 0$), then

Step size: $$\Delta x \cong h|q| = (\frac{27eh^6}{4Edt^3})^{\frac{1}{4}}\sqrt{V} \tag{1-9}$$

Another approach used a second-order differential equation [8] to predict the snap through and priming voltages by using square load model in Figure 1-6. The results are as following

Snap through (pull-in) voltage V_{pi} =

$$\frac{EI}{Wek_1L^2}\frac{\{(6Wek_1/dEI)[2d(Z_m + 3(Kd/L)/Z_m(Z_m - d)) - (3\sqrt{d/Z_m})\tanh^{-1}\sqrt{d/Z_m} - \ln(Z_m - d/Z_m)]\}^{1/2}}{((1/d) + (3K/Z_mL))(1/Z_m - d) - (3/2d\sqrt{Z_md})\tanh^{-1}\sqrt{d/Z_m} - (1/2d^2)\ln(Z_m - d/Z_m)} \tag{1-10}$$

Priming voltage V_{pr} =

$$[\frac{24Z_b^2EI}{ek_2L^4W}(\frac{3}{\sqrt{Z_nZ_b}}\tan^{-1}(\frac{Z_b}{\sqrt{Z_nZ_b}}) - \frac{\ln(Z_n + Z_b)}{Z_b} - \frac{2}{Z_n} + \ln Z_n)]^{1/2} \tag{1-11}$$

Other works on the determination of deflection and step size [21, 22] followed basically the piecewise combination of previous methods [2, 8, and 19] with minor modifications and the results were like that of previous literatures. For the step size with variable load, such as SDA connected to a suspended spring under continuous loading/unloading process, was not reported yet. The increasing spring force will decrease the step size dynamically. As the driving voltage continuously input, the total travel distance is accumulated also and represented the positioning ability of SDA device.

For the determination of SDA output force, experimental approaches have been reported mainly. These methods include buckling-load method [1] and spring-deflection method [8, 23] as shown in Figure 1-7. The output force of SDA array in Figure 1-7(a) is expressed as the buckling load of the slender buckle beam, which is related to the geometry, material and constraint type of the beam. The test results [1] showed that the buckle beam sometimes bifurcated into two different mode shapes; as a result, the output force was not easily determined as one unique value. In Figure 1-7(b), the SDA output force is determined as the multiplication of the spring constant and its total deflection. Arranging and classifying results in previous literatures, some key characteristics and performances are listed in Table 1. It is clear that till now, no analytical formulations are reported to be able to model completely both the static and the dynamic behavior of SDA including friction effect.

1.3 Goals

From the discussion above, the goals of this work may be ascribed into two major topics. The first one is to propose a better analytical model on SDA to improve the prediction capability such as priming voltage, step size, total travel distance, output force and dynamic response simulation. The second one is to propose a novel lower voltage SDA (LVSDA) design in comparison with higher driving voltage of conventional rectangular SDA to extend the

compatibility of SDA with integrated circuit process.

1.4 Approach in this study

To achieve research goals of this work, the current approach is stated as following. In chapter 1, the motivation is first declared and followed by a comprehensive literature review of SDA and related topics. Then the goals are introduced and followed with detail description on research methods and procedures. In chapter 2, a unified analytical method for improved SDA modeling is proposed and derived in sequence. Governing differential equation of fourth-order is presented based on Euler-Bernoulli beam and distributed electrostatic load. From this equation, much valuable information may be extracted in systematic manner; such as deflection curve, step size, bending moment, maximum stress and output force. The output force data just derived is applied into a single degree of freedom model of SDA. By simulating its vibrational motion, total travel distance and dynamic output force can be determined numerically for the first time under given parameters of mass, friction, spring constant and input voltage.

In chapter 3, a novel flexible joint design is proposed to incorporate into the conventional SDA design to improve performance in low-voltage region due to the smaller flexural rigidity. This novel design of lower voltage scratch drive actuator (LVSDA) is confirmed by qualitative analysis and finite element analyses on stress distribution and deformation of test structures. In chapter 4, micro-electroplated nickel SDA and LVSDA arrays connected with suspended spring are fabricated by a two-mask process developed in NCTU. Then the released devices are tested to verify capability of the proposed SDA model and novel LVSDA design with analytical and simulated results. The test results show good agreement between the prediction of improved SDA model with experiment data, including total travel distance and output force. Because the step size is in nanometer range, as its measurement is not as easier as the measurement of total travel distance on the basis of thousands of input pulses, the step size

measurement is in stead of total travel distance. The test results also show that the LVSDA can operate well even at as low as 40 volts, a 50% reduction than 80 volts of SDA, which can not be done by conventional rectangular SDA with the same size. In chapter 5, the major contributions of this work are summarized and the future works are also discussed in brief.

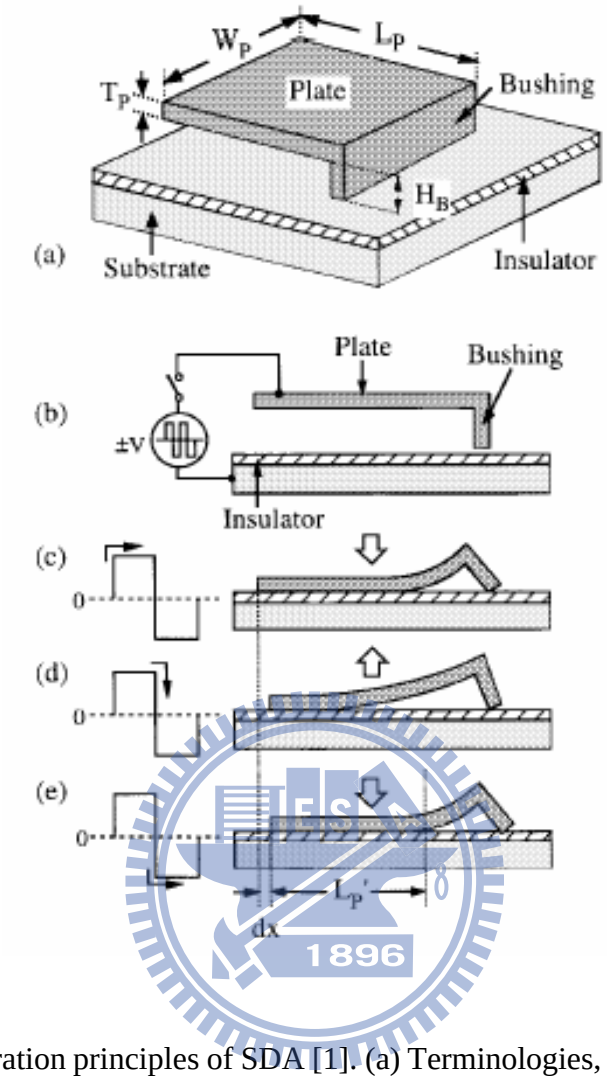

Figure 1-1. Operation principles of SDA [1]. (a) Terminologies, (b) SDA placed on insulator and substrate, driven by voltage pulse in capacitor circuit, (c) Positive signal, main plate priming, bushing scratches ahead, (d) Low signal, main plate spring back and sliding forward, (e) Negative signal, main plate priming again, bushing scratches ahead

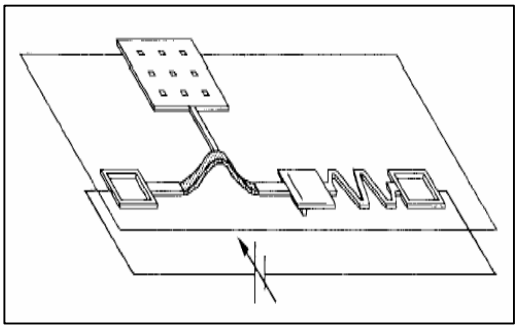

(a) Concept of micro-assembly [1].

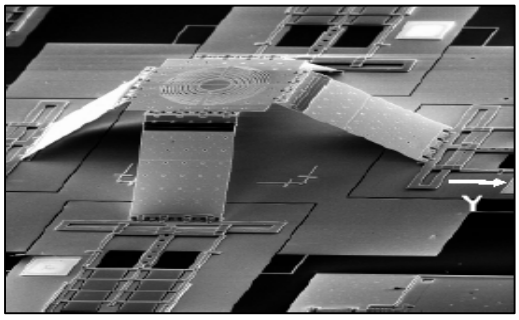

(b) Optical xyz-stage assembly [5].

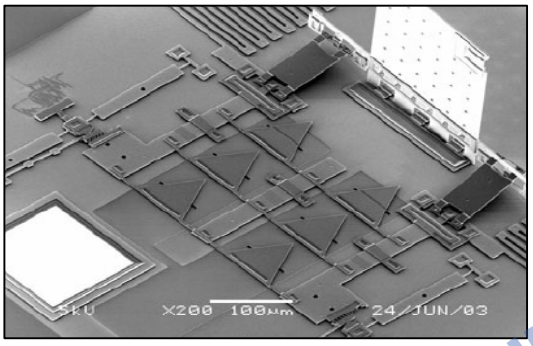

(c) Variable Optical Attenuator assembly [6].

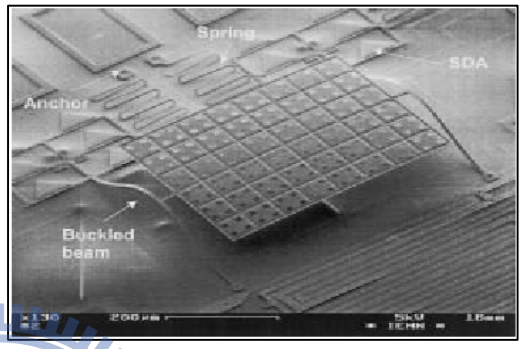

(d) Platform assembly [7]

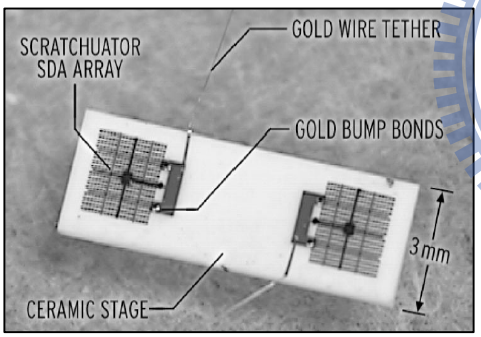

(e) Microrobot actuated [8].

(f) Cam-motor [9].

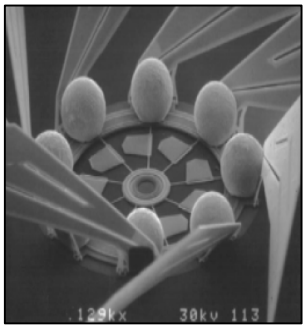

(g) Micro-fan [10].

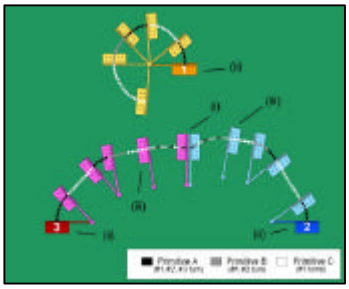

(h) Wireless microrobot [13].

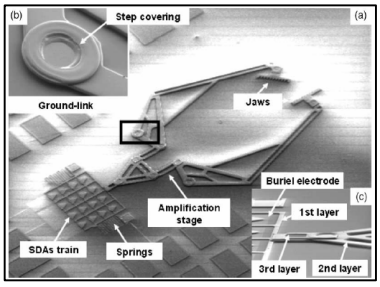

(i) Micro-gripper[16].

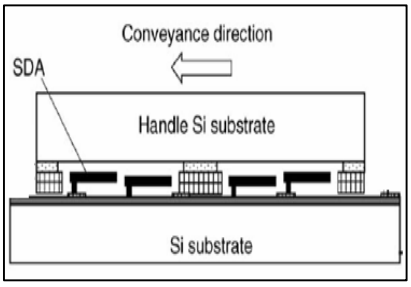

(j) Micro-translation table [17].

Figure 1-2. Typical applications of SDA in microelectromechanical system (MEMS).

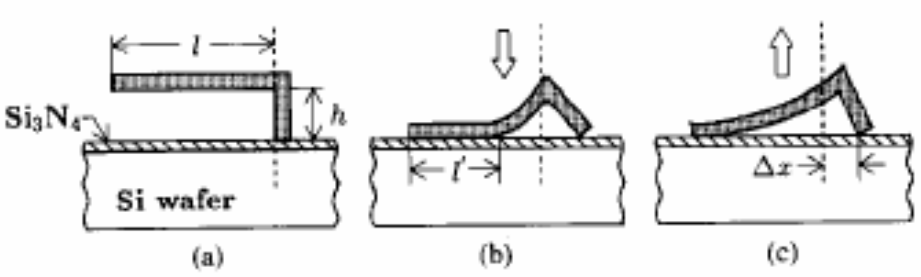

Figure 1-3. Step size estimated from experimental results in Akiyama's work [2].

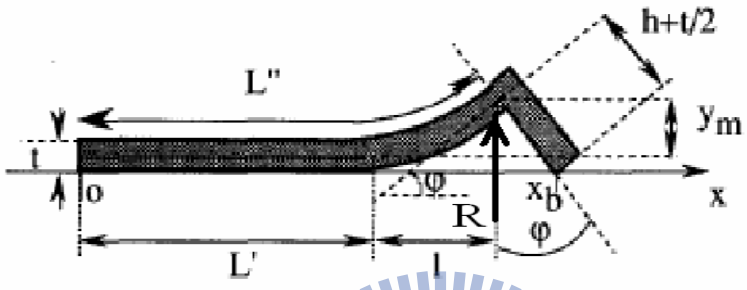

Figure 1-4. Step size estimated from experimental results in Langlet's work [19].

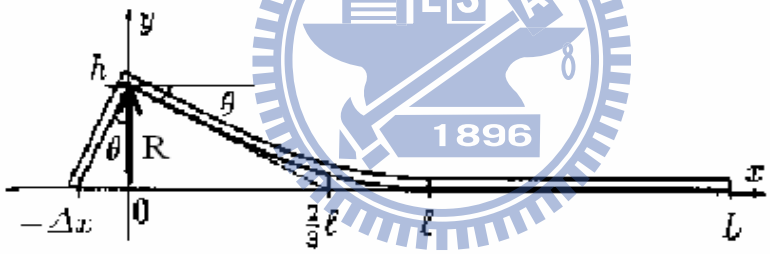

Figure 1-5. Step size predicted from analytical model in Kazuaki's work [20].

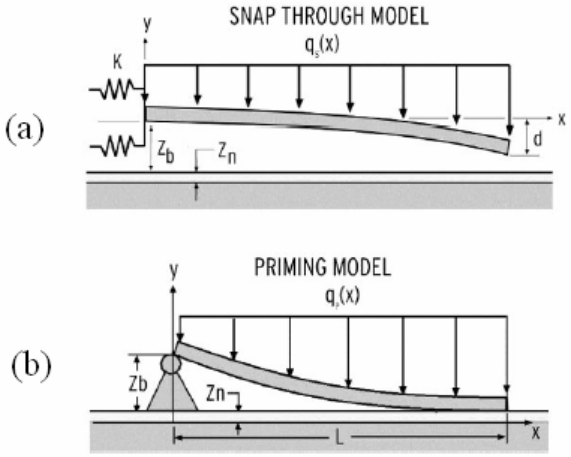

Figure 1-6. Snap through voltage (a) and priming voltage predicted from analytical model in Linderman's work [8].

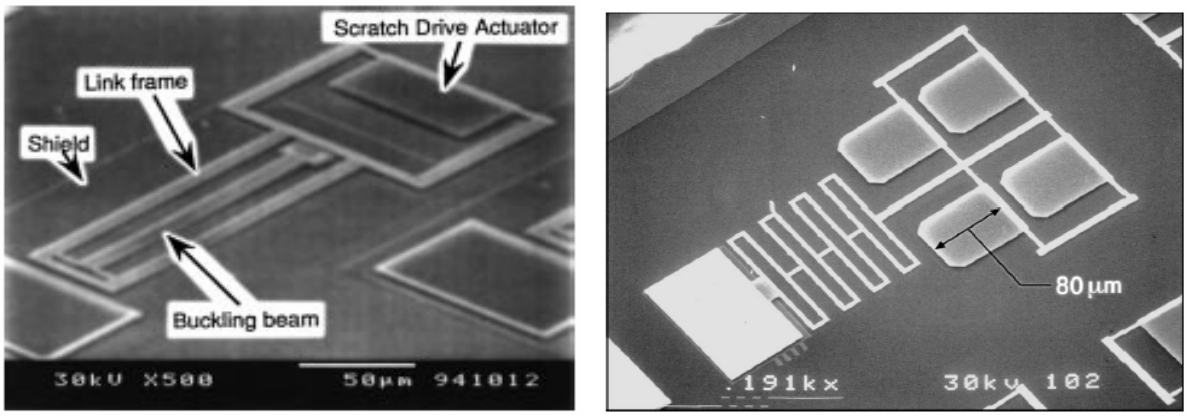

Figure 1-7. Output force estimation methods. (a) Buckling beam method in Akiyama's work [1], (b) Tether spring method proposed in Linderman's work [8] and Li's work [23] respectively.

Table 1-1. Summary of previous researches on SDA modeling

Property / Reference	Priming voltage	Non-contact length	Step size	Traveling distance	Output force	Dynamical simulation
Akiyama,1993 [2]	**No**	**after testing***	**after testing**	**after testing**	**No**	**No**
Langlet, 1997 [19]	**No**	**after testing**	**after testing**	**after testing**	**No**	**No**
Akiyama,1997 [1]	**No**	**after testing**	**after testing**	**after testing**	**after testing**	**No**
Kazuaki,1998 [20]	**No**	**Yes**	**Yes**	**No**	**No**	**No**
Linderman, 2001 [8]	**Yes**	**No**	**after testing**	**after testing**	**after testing**	**No**
This work	**Yes**	**Yes**	**Yes**	**Yes**	**Yes**	**Yes**

Note: "after testing" means the property is estimated after testing has been done.

Chapter 2 Modeling of Scratch Drive Actuator

The typical structures of SDA are shown in Figure 2-1(a). One usual constraint type at the contact part of support beams with rail is a slider joint without rotation as in Figure 2-1(b) [23]. A systematic approach will be proposed to analyze the static and dynamic behavior of SDA.

2.1 Operation principle of SDA

The operation of SDA from rest to scratch forward is classified into five states shown in Figure 2-2. As the input voltage V increases from zero, the still SDA in Figure 2-2(a) starts rotating about the bushing paw and the free edge of main beam just touches the dielectrics at the pull-in voltage V_{pi} as in Figure 2-2(b). For input higher than pull-in voltage V_{pi}, the main beam will be bent and gradually becomes a surface contact with the dielectrics as Figure 2-2(c), so-called priming voltage V_{pr}. After that, the contact length of main beam to the dielectrics increases as input voltage increases, it is so-called post-priming at voltage V_{pp}, as shown in Figure 2-2(d). Finally, when the input voltage is fully discharged, the SDA will spring back and keep the one forward step, as shown in Figure 2-2(e).

2.2 Static analysis of SDA

Some assumptions are made first before the derivation. **The deformation and electrostatic force are assumed to be same along the width direction of SDA, as the main plate may be treated by beam model** [24]. The Euler-Bernoulli beam theory is applied on main plate and support beams; the bushing, dielectrics and rails are assumed to be rigid. The angle between the bushing and main plate remains right angle all over the deformation process, and the electrostatic force acted on bushing is ignored. At pull-in, priming or post-priming state, the contact between main beam and dielectrics remains. In other words, free end of main beam is assumed to be fixed, and only the bushing can deflected and scratch ahead at priming and

post-priming states. In static analysis, it is natural to draw the condition as no slippage occurs during charging and discharging. The vertical displacement of bushing top is negligible during main beam deflection in priming and post-priming states. The fringing effect of electrostatic field is ignored.

For a general parallel plate capacitor, the distributed load q, i.e. the electrostatic force per unit length applied to the plate, is given as

$$q = \frac{e_0 W V^2}{2d^2}, \tag{2-1}$$

where e_0 is the permittivity of air; V is the input voltage; W is the plate width; d is the gap between two plates. Let the SDA be modeled as plate capacitor, d is defined as the distance from the main beam to the electrode on substrate, including air and the dielectric layers. The distance d varies with the deflection y and electrostatic load q. Due to the nonlinear coupling between the electrostatic load q and main beam deflection y, there is not yet an exact solution for the deflection curve y. A square law of deflection has been proposed to define the deflection curve of a cantilever beam under electrostatic force [8]. By combining Euler-Bernoulli beam theory and the square law model, the governing equation of the main beam with the distributed electrostatic load $q(x)$ at post-priming state can be expressed as a fourth-order differential equation:

$$\frac{\mathrm{d}^4 y}{\mathrm{d}x^4} = \frac{q(x)}{EI} = \frac{e_0 W V^2}{EI(a + bx^2)^2}, \tag{2-2}$$

where a is equal to the thickness t of the dielectric layer divided by the relative permittivity k; b is equal to h / l_n^2; l_n is the non-contact length of main beam at the given input voltage; h is the bushing height; E is the Young's modulus of SDA material; I is the second area moment of main beam; x is the horizontal coordinate of the element in consideration. The downward

deflection is defined as positive. The coordinate system is shown in Figure 2-3 where the origin is defined at the juncture point between contact and non-contact regimes with distance *h* above. Integrating equation (2-2) successively four times leads to following equations:

$$\frac{d^3y}{dx^3} = \frac{e_0 W V^2}{EI}\left(\frac{x}{2a(a+bx^2)} + \frac{\tan^{-1}\left(\frac{bx}{(ab)^{1/2}}\right)}{2a(ab)^{1/2}}\right) + c_1, \tag{2-3}$$

$$\frac{d^2y}{dx^2} = \frac{e_0 W V^2}{EI}\left(\frac{\ln a}{4ab} + \frac{x\tan^{-1}\left(\frac{bx}{(ab)^{1/2}}\right)}{2a(ab)^{1/2}}\right) + c_1 x + c_2, \tag{2-4}$$

$$\frac{dy}{dx} = \frac{e_0 W V^2}{EI}\left(\frac{x(\ln a - 1)}{4ab} + \frac{(a+bx^2)\tan^{-1}\left(\frac{bx}{(ab)^{1/2}}\right)}{4(ab)^{3/2}}\right) + \frac{c_1}{2}x^2 + c_2 x + c_3, \tag{2-5}$$

$$y = \frac{e_0 W V^2}{EI}\left(\frac{3\ln a - 2\ln\left(1+\frac{bx^2}{a}\right)}{24b^2} + \frac{3x^2\ln a - 4x^2}{24ab} + \frac{(3ax+bx^3)\tan^{-1}\left(\frac{bx}{(ab)^{1/2}}\right)}{12(ab)^{3/2}}\right)$$
$$+ \frac{c_1}{6}x^3 + \frac{c_2}{2}x^2 + c_3 x + c_4, \tag{2-6}$$

The four integration constants, c_1, c_2, c_3, c_4 and non-contact length l_n, can be solved with the following five boundary conditions:

$$y(0) = h, \tag{2-7}$$
$$y'(0) = 0, \tag{2-8}$$
$$y''(0) = 0, \tag{2-9}$$
$$y(l_n) = 0, \tag{2-10}$$
$$k_t y'(l_n) = EIy''(l_n). \tag{2-11}$$

Eq. (2-7) means the y position of origin remains to be the bushing height, h. Also, the contact region is flat and fixed to the dielectrics at post-priming state, so the slope and moment at origin O are zero, as implied by Eq. (2-8) and Eq. (2-9), respectively. Eq. (2-10) states that the vertical displacement of bushing is negligible. Eq. (2-11) expresses the balance between the moment $EIy''(l_n)$ of main beam and the torque $k_t y'(l_n)$ from the support beam at $x = l_n$. The parameter k_t is the torsional spring constant of support beam and defined as $2bGW_p t^3/L_p$, where b is an

aspect ratio constant based on the ratio of the width to thickness of the support beam [25]; W_p is the width of support beam; L_p is the length of support beam; G is shear modulus of SDA material.

Applying the boundary condition of Eq. (2-7) to Eq. (2-9) into characteristic equations Eq. (2-4) to Eq. (2-6), the integration constants c_2, c_3 and c_4 can be solved as:

$$c_2 = -\frac{e_0 W V^2}{EI}\frac{\ln a}{4ab}, \tag{2-12}$$

$$c_3 = 0, \tag{2-13}$$

$$c_4 = h - \frac{e_0 W V^2}{EI}\left(\frac{l_n^4 \ln a}{8h^2}\right). \tag{2-14}$$

Applying Eq. (2-10) into characteristic Eq. (2-3), the integration constant c_1 can be solved as:

$$c_1 = \frac{e_0 W V^2}{EI}\left(\frac{1}{abl_n} - \frac{(3a + bl_n^2)\tan^{-1}\left(\frac{bl_n}{(ab)^{1/2}}\right)}{2(ab)^{3/2} l_n^2} + \frac{\ln\left(1+\frac{bl_n^2}{a}\right)}{2b^2 l_n^3}\right) - \frac{6h}{l_n^3}. \tag{2-15}$$

Rewriting the expression of Eq. (2-11) in terms of Eq. (2-4) and Eq. (2-5) can lead to the

$$k_t\left\{\frac{e_0 W V^2}{EI}\left(\frac{-2a\tan^{-1}\left(\frac{bl_n}{(ab)^{1/2}}\right)}{4(ab)^{3/2}} + \frac{\ln\left(1+\frac{bl_n^2}{a}\right)}{4b^2 l_n} + \frac{l_n}{4ab}\right) - \frac{3h}{l_n}\right\}$$

$$= \left\{e_0 W V^2\left[-\frac{3a\tan^{-1}\left(\frac{bl_n}{(ab)^{1/2}}\right)}{2(ab)^{3/2} l_n} + \frac{1}{ab} + \frac{\ln\left(1+\frac{bl_n^2}{a}\right)}{2b^2 l_n^2}\right] - \frac{6EIh}{l_n^2}\right\}. \tag{2-16}$$

characteristic equation of non-contact length l_n for given input V;

Since no explicit solution exists, the non-contact length l_n is solved by numerical method. At the priming state, the not-contact length is considered to be the same as the main beam length L, and then the priming voltage V_{pr} can be determined from reorganizing Eq. (2-16) by replacing l_n with main beam length L as

$$V_{pr} = [\frac{(\frac{3k_t h}{L} - \frac{6EIh}{L^2})}{A_1 - A_2}]^{\frac{1}{2}}, \quad \text{where} \tag{2-17}$$

$$A_1 = \frac{e_0 k_t W}{EI}(\frac{-2a\tan^{-1}(\frac{bL}{(ab)^{1/2}}))}{4(ab)^{3/2}} + \frac{\ln(1+\frac{bL^2}{a})}{4bL} + \frac{L}{4ab}), \tag{2-18}$$

$$A_2 = e_0 W(-\frac{3a\tan^{-1}(\frac{bL}{(ab)^{1/2}})}{2(ab)^{3/2}L} + \frac{1}{ab} + \frac{\ln(1+\frac{bL^2}{a})}{2b^2L^2}). \tag{2-19}$$

By definition, the bending moment M at any position x in non-contact part of main beam is

$$M = -EI\frac{d^2y}{dx^2} = e_0 WV^2[\frac{bl_n^2 x(-\tan^{-1}(\frac{bx}{(ab)^{1/2}}) + \tan^{-1}(\frac{bl_n}{(ab)^{1/2}})) + 3ax\tan^{-1}(\frac{bl_n}{(ab)^{1/2}})}{2(ab^2)^{3/2}l_n^2}$$

$$-\frac{x}{abl_n}\frac{x\ln(1+\frac{bl_n^2}{a})}{2b^2l_n^3}] + \frac{6EIh}{l_n^3}x. \tag{2-20}$$

given by definition as following where flexural rigidity EI is constant

There are two methods to determine the position x_{max} where the maximum moment M_{max} happens along main beam for a specific input voltage. The first one is to decide the coordinate that the shear force, $-EI(dy/dx)$, becomes zero. Then substituting this coordinate into Eq. (2-20) will find the maximum moment. The one is straight forward in applying the optimization toolbox in Matlab to find out the extreme value along main beam. The maximum bending stress

$$s_{max} = \frac{6M_{max}}{Wt^2} \tag{2-21}$$

s_{max} along main beam for corresponding input can be expressed as:

The horizontal output force F_o of charged SDA array along the main beam varies with the input voltage. The friction force along contact regime is assumed to be large enough to keep the contact area stationary. The horizontal output force F_o is basically the horizontal component of

the electrostatic force along main beam. It can be solved by integrating the horizontal component of electrostatic force along the non-contact part as:

$$F_o = N\int_0^{ln} \frac{e_0 W V^2 \sin q}{(a+bx^2)^2}\,dx, \qquad (2\text{-}22)$$

where N is the SDA number in the SDA array, q is the angle between the horizontal and the tangent line along main beam, and can be calculated from the slope of deflection curve.

In order to recognize SDA step size in fully discharge mode, Figure 2-4 shows the SDA deflection and displacement of bushing from still, charge and discharge. At pull-in voltage, the SDA rotates about bushing paw. Due to the slope change on bushing, the bushing top moves back horizontally with magnitude $\triangle x_1 = h*sin(tan^{-1}(h/L))$, as shown in Figure 2-4(a). When the input voltage is equal to or larger than the priming voltage, the main beam starts bending and causes the bushing top to move backward more due to so-called curvature shortening effect, which has not been considered in previous literatures on SDA. The lateral displacement due to curvature shortening effect can be formulated as $\triangle x_2 = \frac{1}{2}\int_0^{ln} (\frac{dy}{dx})^2 dx$ in Figure 2-4(b) [25]. This effect will make the bushing rotate more in counterclockwise, and then the bushing paw moves forward for certain horizontal distance given by $\triangle x_3 = h*\left|\, dy/dx \,\right|$ as shown in Figure 2-4(c). When SDA is fully discharged, the main beam will spring back and rotate about the bushing paw as Figure 2-4(d). By combining the net effect of three above effects, the step size in this type of SDA motion control becomes

$$\begin{aligned}\Delta x &= \Delta x_3 - \Delta x_1 - \Delta x_2 \\ &= h*\left(\left|\frac{dy}{dx}\right|_{bushing} - \sin(\tan^{-1}\frac{h}{L})\right) - \frac{1}{2}\int_0^{ln}(\frac{dy}{dx})^2 dx\end{aligned} \qquad (2\text{-}23)$$

The weakness of driving method in Figure 2-4 is that the main beam may rotate too much. As a result, SDA is possible to turn over or not easy to pull back by electrostatic force

immediately. An effective alternate driving method is to keep the main beam constantly contact with dielectrics under input levels V_P and V_{PP} between priming and some post-priming input.

$$\Delta x = \Delta x_{pp} - \Delta x_p \qquad (2 - 24)$$

Figure 2-5 shows the components of step size in this driving mode, i.e., constantly contact mode. As the slope effect Δx_1 is avoided, the net step size Δx may be simplified as

the step size at input voltage V_{PP}, Δx_{pp} minus the step size at input voltage V_P , Δx_p.

2.3 Dynamic analysis of SDA

To explore the dynamic behavior of SDA including friction effect, a mass-spring-damper model of single degree of freedom (SDOF) is proposed as an approximation. The equation of motion and its normalized form are given as Eq. (2-25) and Eq. (2-26)

$$m\ddot{x} + c\dot{x} + mF_N sign(\dot{x}) + kx = F_O * abs(\sin(w\,t)) \qquad (2\text{-}25)$$

$$\ddot{x} + \frac{c}{m}\dot{x} + \frac{mF_N}{m} sign(\dot{x}) + \frac{k}{m}x = \frac{F_O}{m} * abs(\sin(wt)) \qquad (2\text{-}26)$$

The coordinate x and its first and second derivatives of with respect to time are the displacement, velocity and acceleration of SDA, respectively. The lump-mass m defines the total mass of SDA array including the ring around SDA. The coefficient k defines the spring constant of the suspended tether spring. The damper may contain one or two types of friction; the first is viscous damping of coefficient c of contact surface between main beam and insulated layer. The second one is the Coulomb friction of coefficient μ accounting for the stick-slip phenomenon in contact surfaces. The force F_N is the normal force between the contact area of main beam and insulated layer. In MEMS, the body force such as gravity force is often much less than surface traction force as the electrostatic force. So the normal force is simplified to contain only the electrostatic force in the contact area. The force F_O is the amplitude of driving force which is the resultant horizontal component of the electrostatic force applied along the main beam of SDA, the force along bushing is ignored here. The driving voltage is in sinusoidal wave sin(wt) of angular velocity w. However, it should be noted that the electrostatic force is an attractive force between contact surfaces, no matter the charge on main beam is positive or negative. Therefore, the driving force is expressed as the absolute value of driving voltage waveform, i.e., abs(sin(wt)) multiplying F_O, which is the motive force that makes SDA scratch forward. The friction terms in Eq. (2-25) may be and rearranged as following

$$\frac{c}{m}\dot{x} + \frac{mF_N}{m} sign(\dot{x}) = sign(\dot{x}) * (gain * abs(\dot{x}) + offset) \qquad (2-27)$$

In Eq. (2-27), sign(~) is the sign function result of the operand in parenthesis; the gain (c/m) is defined as a regulation factor that modifies viscous friction coefficient. The offset (mF_N/m) is the dry friction force that should be overcome in motion. To simplify the derivation, the static and dynamic dry friction coefficients are assumed to be same as m.

When the Coulomb friction is activated, the analysis of displacement (total travel distance) response is too complex to derive an exact and compact analytical solution. To solve this type of nonlinear vibration problems, some methods have been developed such as perturbation method, averaging method, multiple scales method and direct separation of motions [26-30]. Instead of these methods, direct numerical simulation method as Simulink™ in Matlab™ has been adopted to investigate the dynamic response in a straight forward way to simulate the dynamical behavior of SDA.

To evaluate the fatigue behavior of SDA, the information of stress bounds are needed. Eq. (2-21) may calculate the maximum and minimum stresses as following

$$s_{max} = \frac{6M_{max}}{Wt^2}, \quad s_{min} = \frac{6M_{min}}{Wt^2} \qquad (2-28)$$

The equivalent stress σ_R, the fully reverse stress of same fatigue life [31], is expressed as

$$s_R = s_{av} + \frac{s_{ult}}{s_e} s_r \qquad (2-29)$$

where

$$s_{av} = \frac{s_{max} + s_{min}}{2}, \quad s_r = \frac{s_{max} - s_{min}}{2}. \qquad (2-30)$$

The minimum moment M_{min} at specific input, though not easily be derived, lies between zero for fully discharge mode and the maximum moment at V_p in constantly contact mode.

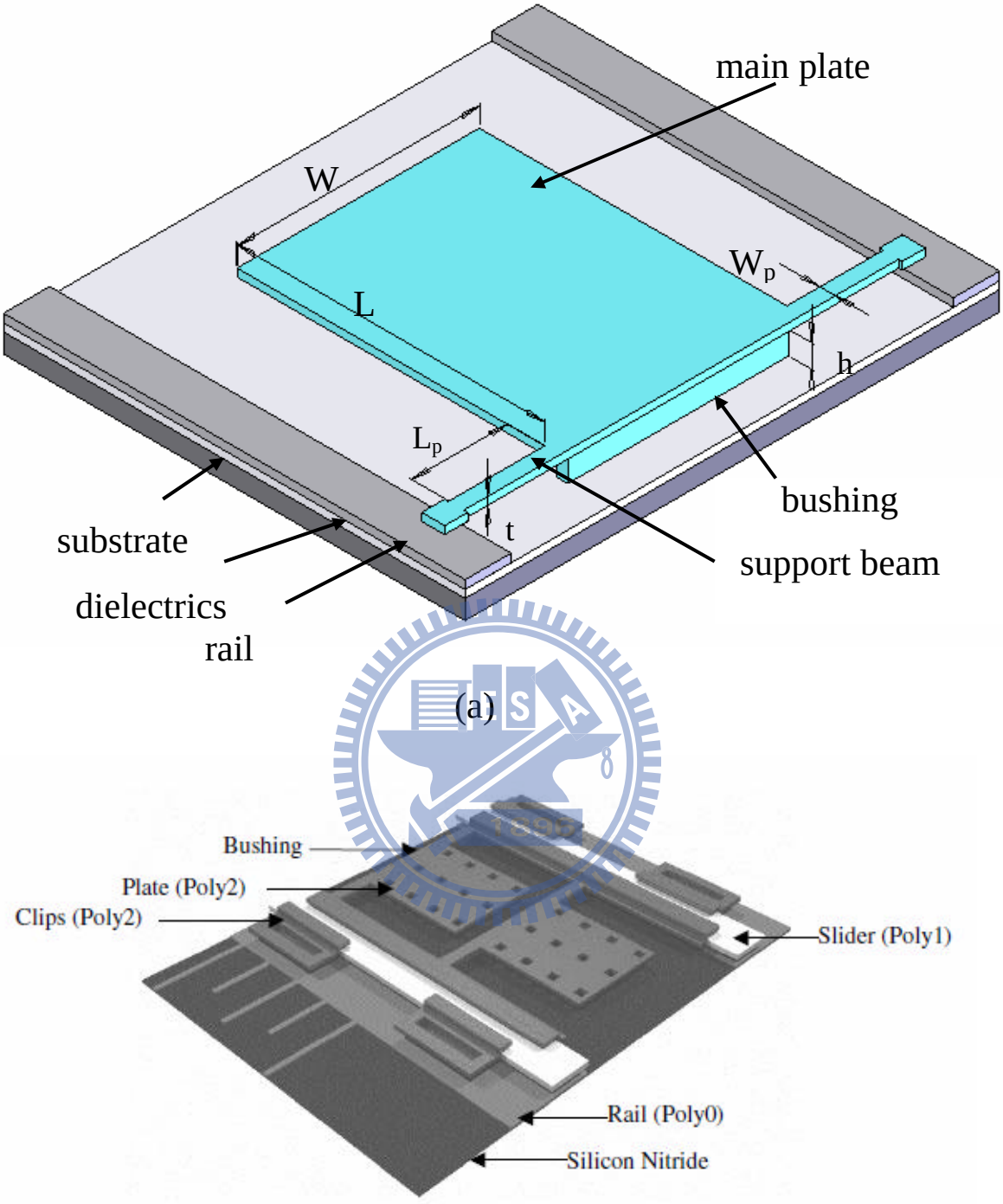

Figure 2-1. Structures and elements of SDA. (a) Support beams are free at contact part. (b) contact part is constrained to slide without rotation [24].

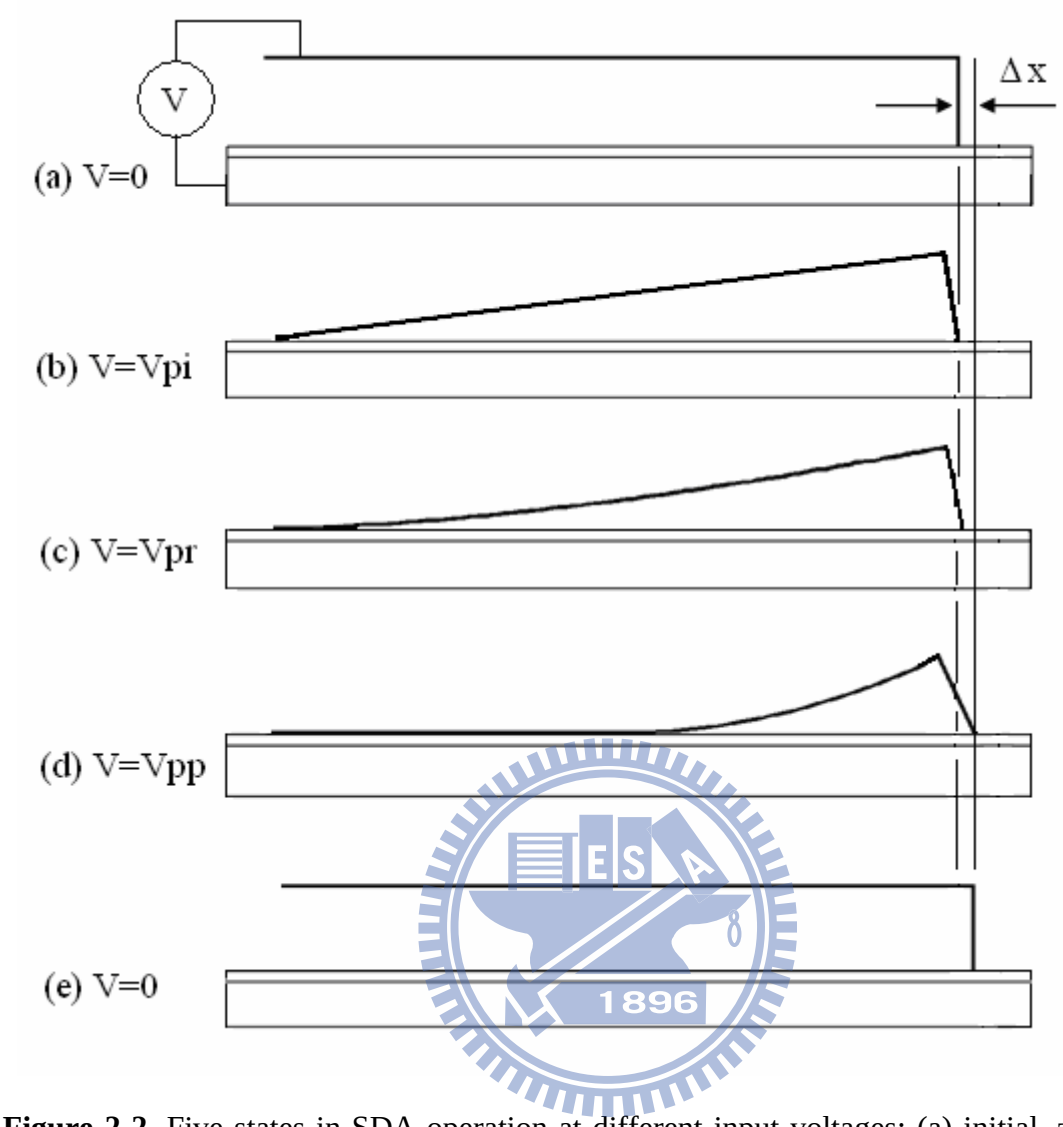

Figure 2-2. Five states in SDA operation at different input voltages: (a) initial, zero input; (b) pull-in, voltage V_{pi}; (c) priming, voltage V_{pr}; (d) post-priming, voltage V_{pp}; (e) one-step forward after discharge.

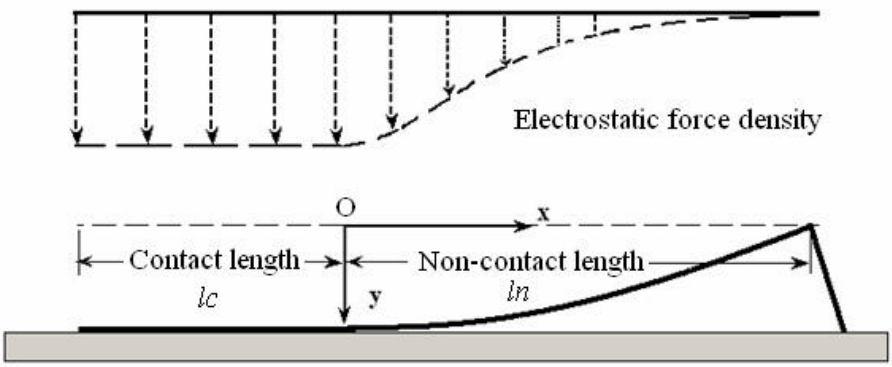

Figure 2-3. Coordinate system and electrostatic force density in post-priming configuration. The electrostatic force density in contact region is constant. In non-contact region, the electrostatic force density follows Petersen model [8].

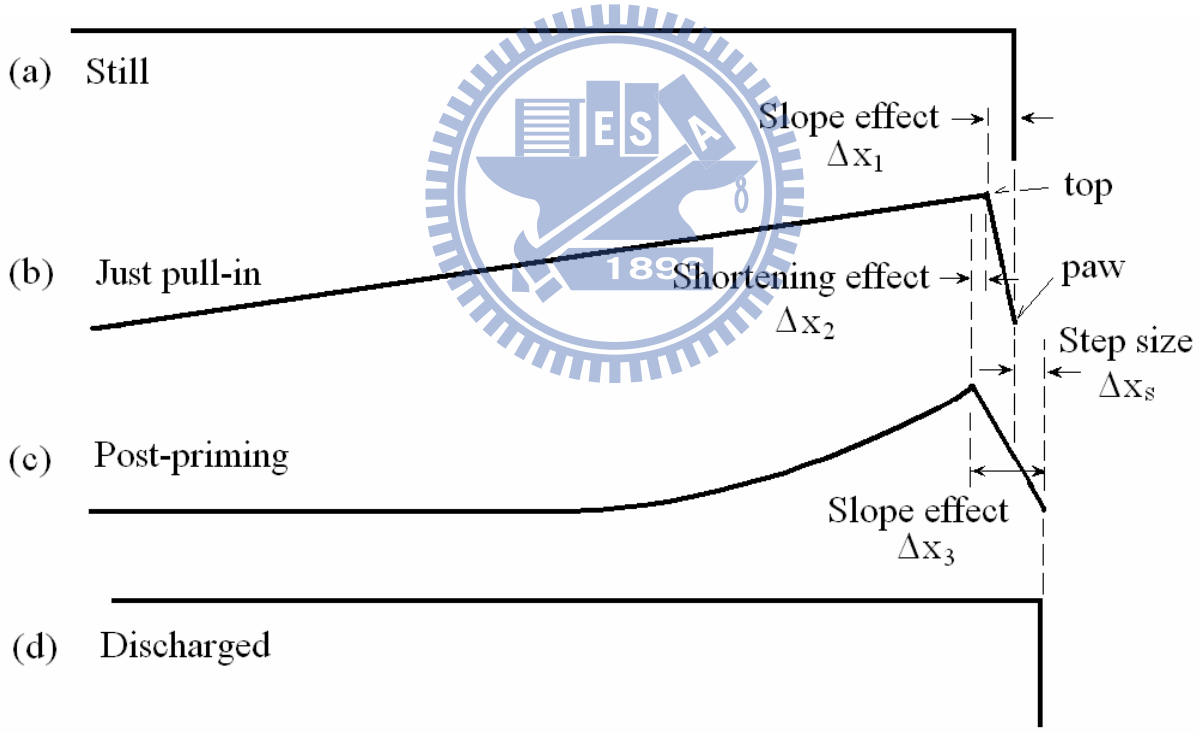

Figure 2-4. Step size of SDA operated in fully-discharge mode. (a) Initial state. (b) The main plate rotates around bushing paw and causes lateral backward movement Δx_1. (c) The curvature shortening effect causes the bushing top lateral movement Δx_2 backward more. Also, the bushing paw displaces Δx_3 forward. (d) SDA is discharged fully with one net step size $\Delta x = \Delta x_3 - \Delta x_1 - \Delta x_2$.

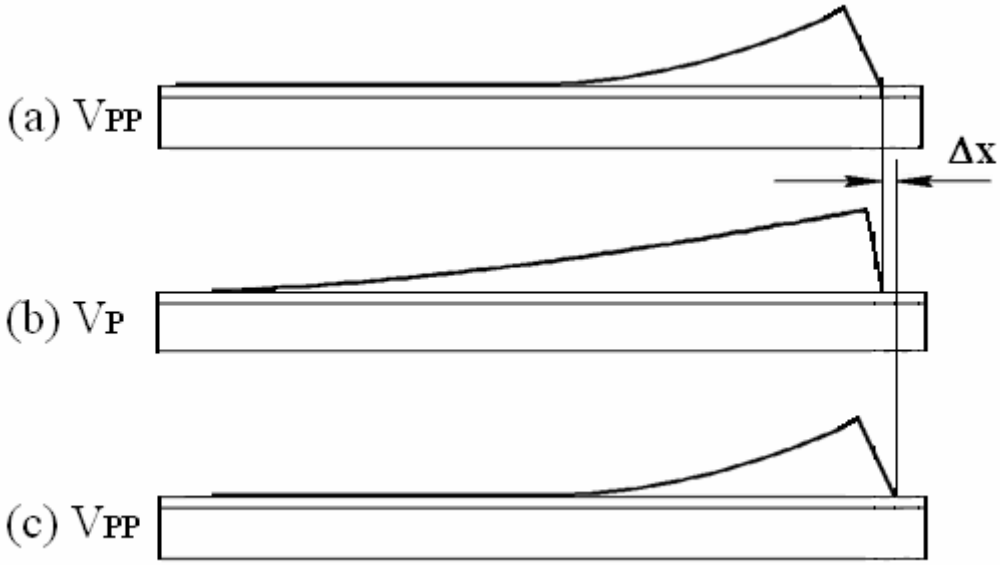

Figure 2-5. Step size of SDA operated in constantly-contact mode. (a) Initial state at voltage V_{PP}. (b) Partly discharge to voltage V_P , main plate springs back. (c) SDA is again charged to V_{PP}, the step size $\Delta x = \Delta x(V_{PP}) - \Delta x(V_P)$.

Chapter 3
Performance Enhancement of Scratch Drive Actuator with Modified Flexible Joint

3.1 Concept design of low voltage Scratch Drive Actuator (LVSDA)

The concept design of the proposed LVSDA is shown in Figure 3-1, where two narrow beams as flexible joint are placed between the main plate and scratch plate. The operation procedures of LVSDA and conventional SDA are illustrated in Figure 3-2. They are both at rest initially with zero input in Figure 3-2(a). When the input increases to snap-through voltage, the free edge of main plate of LVSDA or SDA will touch the dielectrics (Figure 3-2(b)). At the same input voltage, LVSDA will snap through more due to the smaller flexural rigidity to generate a larger bushing lateral displacement, as shown in Figure 3-2(b). At an even higher input voltage, the main plate will contact with the dielectrics more area and further push the bushing forward, as Figure 3-2(c). After discharging, LVSDA or SDA will bounce back to complete one cycle with one forward step size Δx, as Figure 3-2(d).

In order to fabricate and test the proposed LVSDA, the geometric parameters in LVSDA are defined in Figure 3-3(a). The design of testing device is illustrated in Figure 3-3(b), where a tether spring consisted of four box springs links four LVSDAs to the contact electrode. The comparison between the proposed LVSDA and conventional SDA is based on the same device size. It means all LVSDAs and SDAs here have the same total plate length L and plate width W, which are fixed as 80 μm and 65 μm, respectively.

L will remain to be 80 μm, as well as the plate length of SDA. The thickness t of plate, spring, and support beams, as well as the bushing height, of LVSDA and SDA is all set at 2 μm. Each support beam has length L_p= 25 μm and width W_p= 3 μm. Different flexible joint

dimensions and locations are designed to investigate their effects on performance. A shorter or wider flexible joint will provide a more rigid joint. Two different flexible joint widths W_j are designed as 6 μm and 12 μm. The designed flexible joint length L_j includes 15 μm and 20 μm. The designed scratch plate length L_s includes 10 μm, 15 μm, and 20 μm. A shorter L_s means the flexible joint is closer to the bushing. Due to different combinations on scratch plate length and flexible joint length, the corresponding main plate length L_m of LVSDA includes 50 μm, 45 μm and 40 μm to keep the total plate length as 80 μm. The designed LVSDA dimensions are denoted as LV-L_s-L_j-L_m-W_j. For example, the test device expressed as LV-10-20-50-12 has following dimensions: L_s=10 μm, L_j=20 μm, L_m=50 μm, and W_j=12 μm. Eight types of LVSDA used in this work are listed in Table 3-1.

The spring constant of one box spring can be expressed as [24]:

$$k_1 = EtW_r^3/(L_r^3), \tag{3-1}$$

where E is the Young's modulus of spring material, t and W_r are the thickness and width of spring beam, respectively, and L_r is the half length of box spring. For the tether spring composed of 4 box springs, the equivalent spring constant becomes

$$k = EtW_r^3/(4L_r^3), \tag{3-2}$$

The output force of LVSDA or SDA can be determined from the result of spring constant multiplied by the deflection of spring.

3.2 Qualitative Analysis of LVSDA

In order to analyze the deflection of LVSDA under given input, a detailed free body diagram for input between snap-through and priming is plotted in Figure 3-4. The equivalent electrostatic force is labeled as F_E. To satisfy this demand, the flexural rigidity EI should

decrease or the moment should increase. As the increasing of moment needs increasing the input which violates the purpose of low-voltage, the reasonable way is to reduce the flexural rigidity EI of the device. By decreasing EI, the LVSDA can be deflected to provide certain force at lower voltage than SDA. In other words, the electrostatic force to resist the mechanical force can be reduced.

3.3 Finite element analysis of LVSDA

The finite element analysis is realized by SolidWorks® and CosmosWorks®. The behavior of LVSDA has been analyzed in detail and will be compared with the experimental results. For stress simulations, since plastic deformation may happen in flexible joint at high driving voltage, the finite element analysis (FEA) in this work are performed by elasto-plastic model in nonlinear static analysis package of CosmosWorks®. According to the material properties of micro electroplated nickel [26-29], the Young's modulus E is selected as 171 GPa, yielding stress is 323 MPa and tangent modulus in plastic region is assigned as 17.1 MPa. The fatigue stress is 195 MPa, and the ultimate stress is 560 MPa. Parameters used in FEA are listed in Table 3-2. The solid modeling process is first to sketch the main body of LVSDA and substrate separately, combining them as assembly with suitable conditions. Then apply material properties to each part; assign constraints according to requirements; apply electrostatic pressure and external load, the pressure is specific for every input voltage. Assign contact conditions on faces that may contact each other during loading, the no-penetration condition is the most important setting to make sure the LVSDA will not penetrate into the ground layer. The meshing size of element often uses default value or even finer value; the results always converge at about 1.0e-3 level. The friction coefficient between contact surfaces is set as 0.2 in all cases.

The electrostatic force on scratch plate, flexible joint, support beams and bushing are neglected. The left edge of main plate is set to be pinned with the dielectric layer and no penetration is allowed. The electrostatic pressure for a given input voltage is approximated by the parallel capacitor model for each strip of 2.5 μm along the main plate. Then stress in the test structure and the contact length between main plate surface and dielectric layer at different input voltages can be simulated. In simulations, the input voltage starts from 40 volts to 120 volts with increment of 10 volts, since all measured threshold voltages are at least 40 volts. A typical simulated result from the CosmosWorks® is shown in Figure 3-5 for device LV-20-20-40-6 at 70 volts. It is found that the maximum stress happens around flexible joint corner next to the main plate and exceeds the yielding stress (Figure 3-5(a)). The contact length between the main plate and dielectric layer is about 20 μm (Figure 3-5(b)). The fully-discharge shape is shown in Figure 3-5(c), in which permanent vertical displacement due to plastic deformation will cause degradation of output force level for same input when yielding begins.

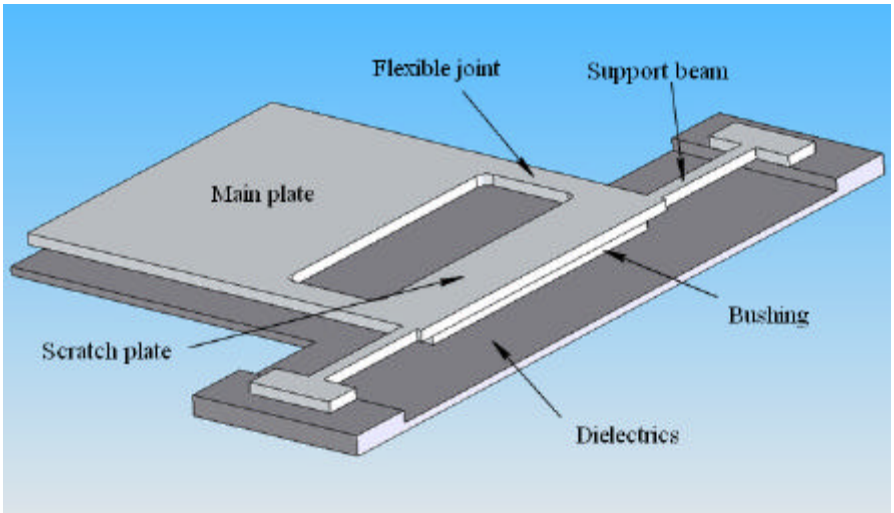

Figure 3-1. Concept design of low-voltage Scratch Drive Actuator (LVSDA) with flexible joint.

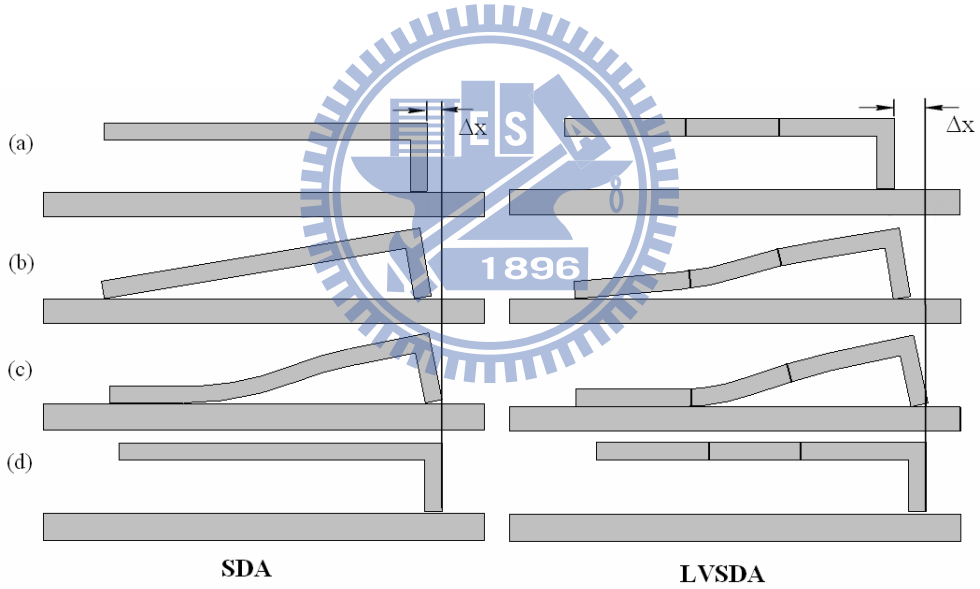

Figure 3-2. Operation procedures of conventional SDA and LVSDA: (a) at rest initially; (b) snap-through ;(c) contact more at higher input voltage; (d) discharge and complete one step size ahead.

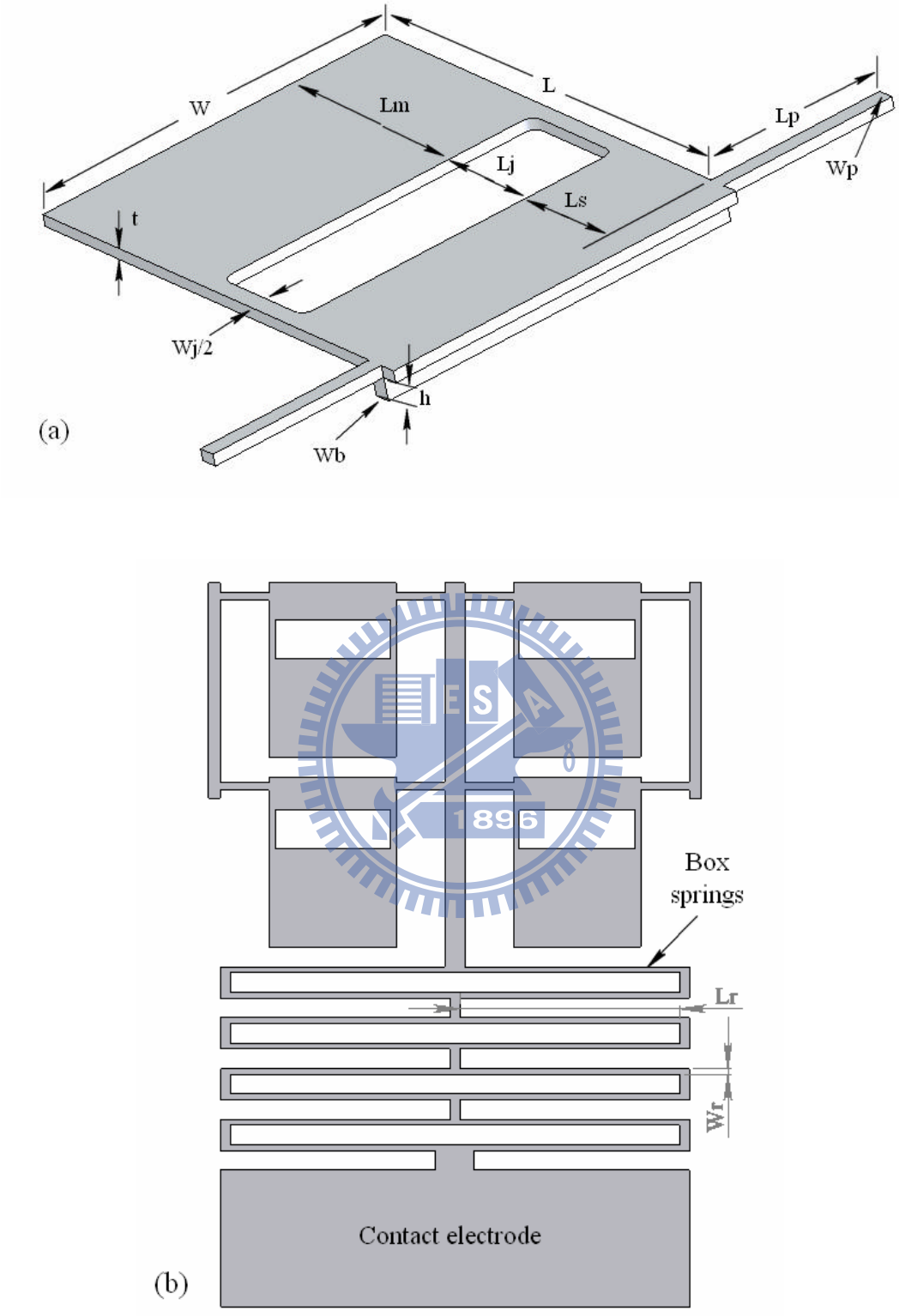

Figure 3-3. Design layout of micro-electroplated nickel SDA. (a) Definition of LVSDA geometric parameters. In another word, the sum of main plate length L_m, flexible joint length L_j and scratch plate length. (b) Four LVSDAs with tether spring connected to the contact electrode.

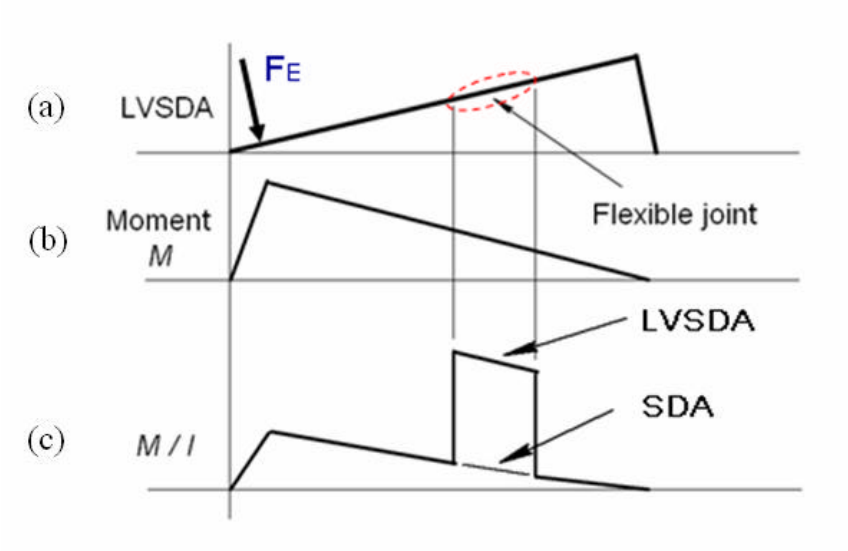

Figure 3-4. Qualitative analysis on flexible joint effect. (a) Equivalent electrostatic force is F_E . (b) Moment *M* along device similar to SDA. (c) (*M/I*) ratio changes hugely along flexible joint in LVSDA. So, the flexible joint reduces flexural rigidity, increases bending stress, induces more deflection and makes LVSDA easier output at lower voltage.

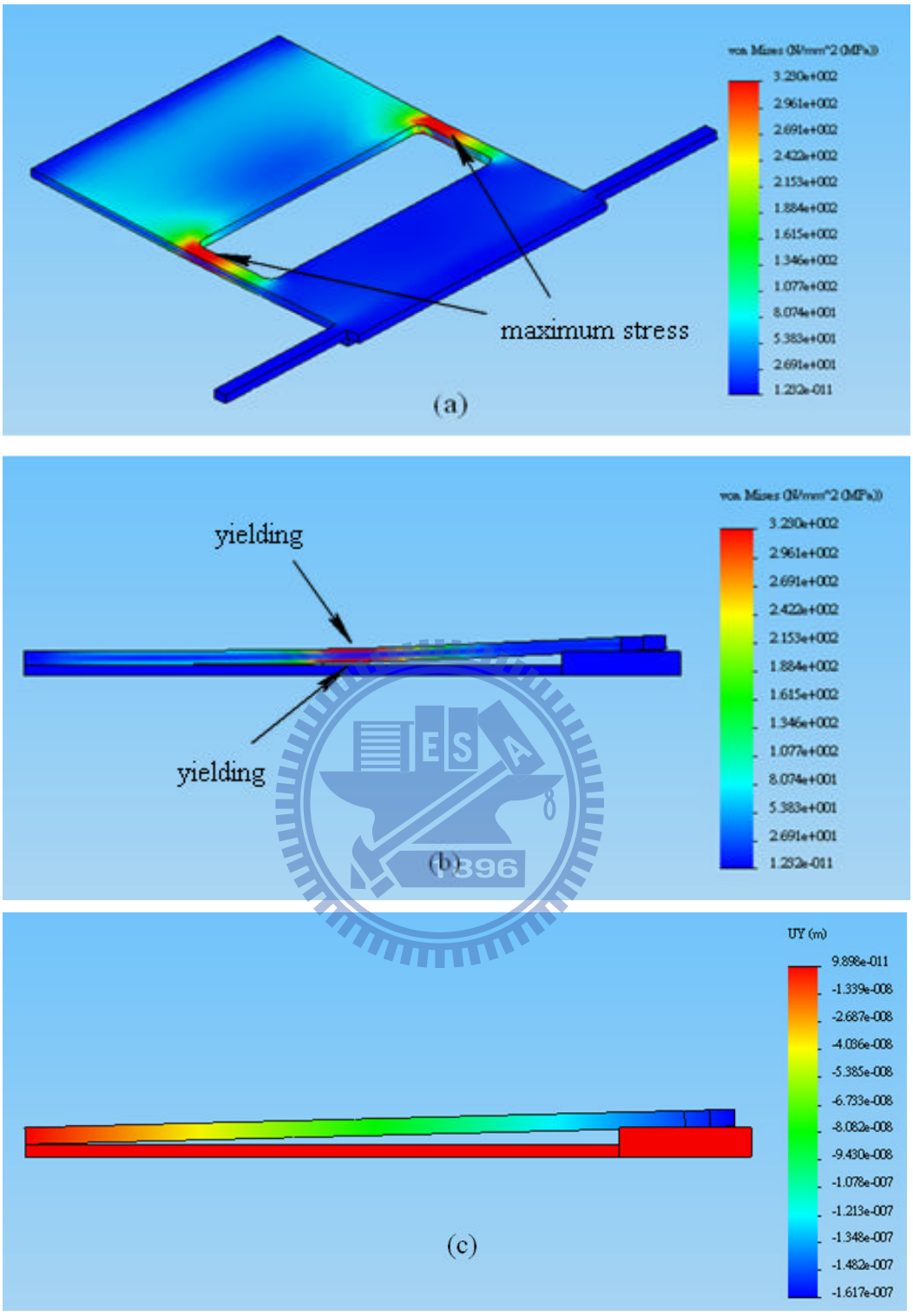

Figure 3-5. Finite Element Analysis (FEA) results of LVSDA with *Ls*=20, *Lj*=20, *Lm*=40 and *Wj*=6 μm (LV-20-20-40-6) at 70 V. (a) Stress distribution, where the maximum von-Mises stress happens at the flexible joint corners close to the main plate. (b) Side view at maximum loading, contact length is about 20 μm. (c) Side view after loading is fully-relax, contact length is about 2 μm. The permanent vertical deflection UY shows plastic deformation at left side on flexible joint that will affect the LVSDA output performance hereafter.

Table 3-1. Notation of LVSDA testing types

Notation **LV-L_s-L_j-L_m-W_j**	**L_s (μm)** Scratch Plate Length	**L_j (μm)** Flexible Joint Length	**L_m (μm)** Main Plate Length	**W_j (μm)** Flexible Joint Width
LV-10-20-50-6	10	20	50	6
LV-10-20-50-12	10	20	50	12
LV-15-15-50-6	15	15	50	6
LV-15-15-50-12	15	15	50	12
LV-15-20-45-6	15	20	45	6
LV-15-20-45-12	15	20	45	12
LV-20-20-40-6	20	20	40	6
LV-20-20-40-12	20	20	40	12

Table 3-2. Simulation parameters for FEA

Parameters	**magnitude**	**Parameters**	**magnitude**
Total main plate length, L, μm	80	Support beam width, W_p, μm	3
Scratch plate length, L_s, μm	10, 15, 20	Plate thickness for all, t, μm	2
Flexible joint length, L_j, μm	15, 20	Bushing height, h, μm	2
Main plate length, L_m, μm	40, 45, 50	Bushing width, W_b, μm	3
Main plate width, W, μm	65	Box spring length, L_r, μm	110
Flexible joint width, W_j, μm	6, 12	Spring beam width, W_r, μm	3
Support beam length, L_p, μm	25	Young's modulus of nickel , E,	171
Spring thickness, same as t,	2	Shear modulus, G, GPa	69
Tether spring constant,	1.98	Yielding stress, σ_y, MPa	323
Tangent modulus, σ_t, MPa	17.1	Element size, μm	2.5
Total nodes	26220	Total elements	15525

Note: The structure material, microelectroplated nickel, is defined as isotropic hardening of von-Mises plasticity once yielding. The solver use sparse matrix of Newton-Raphson method based on force control algorithm.

Chapter 4 Fabrication and Results

In order to verify the validity of the proposed models of SDA and LVSDA, a two-mask micro-electroplated nickel surface-micromachining process is chosen to construct Ni SDA and LVSDA array structures. The test structure is composed of four SDAs or LVSDAs connected to a suspended spring which is anchored to the contact electrode.

4.1 Fabrication process

The fabrication process is summarized as following: (a) Starting from a 4-in. RCA-clean (100) wafer, a 6000Å thick LPCVD silicon nitride is grown in furnace as the dielectric layer (Figure 4-1(a)). (b) First patterning process: coating 2μm photoresist FH6400 as sacrificial layer, 90℃ soft bake 10 minutes, hydration reaction 20 minutes, then creating the pattern of bushing and contact electrode by the first mask (Figure 4-1(b)). (c) Sputtering process: 200Å thick Ti and 1500Å thick Cu are sputtered sequentially as the adhesive layer and seed layer, respectively (Figure 4-1(c)). (d) Second patterning process: coating 5μm thick photoresist AZ9260, then creating the pattern of electroplating mold by the second mask (Figure 4-1(d)). (e) Electroplating nickel process: electroplating the Ni test structure with Watt bath with current density 10 mA/cm^2 over 10 minutes to form 2μm thick Ni (Figure 4-1(e)). (f) Release process: using Acetone to remove electroplating mold AZ9260, then removing Cu seed layer by CR-7T solution about 20 seconds. Ti adhesive layer is then removed by BOE solution about 10 seconds, then the removal of FH6400 sacrificial layer by Acetone for 30 minutes. By immersing in IPA solution and vibrating about 20 seconds for releasing, then drying at 60℃, a fully suspended test Ni structure can be obtained as in Figure 4-1(f). Typical fabricated results are shown in Figure 4-2, including (a) the SDA array, (b) the LVSDA array, (c) close-view of

bushing, and (d) close-view of LVSDA. The lithography parameters are listed I Table 4-1; while the electroplating parameters are listed in Table 4-2 for reference.

The experimental equipments for loading test include an optical microscope mounted with a CCD camera, PC with image process software, chip position table, function generator, high-voltage power amplifier and probe station. The test chip is fixed on the position table by vacuum chuck. Two probes are adjusted to touch the contact electrode of SDA array and substrate. The test signal is generated from the function generator, amplified and calibrated by the high-voltage power amplifier in sinusoidal waveform of 500 Hz. This input is composed of a DC offset at 30 volts often and AC voltage depending on the control command. For example, when the driving signal needs to vary in the range of 30 to 120 volts, the chosen DC offset is 30 volts and AC amplitude is 90 volts in peak to peak definition. The motion of SDA or LVSDA array is recorded by the CCD in computer and then analyzed by using image process software. Typical measurement set-up and driving test are shown in Figure 4-3.

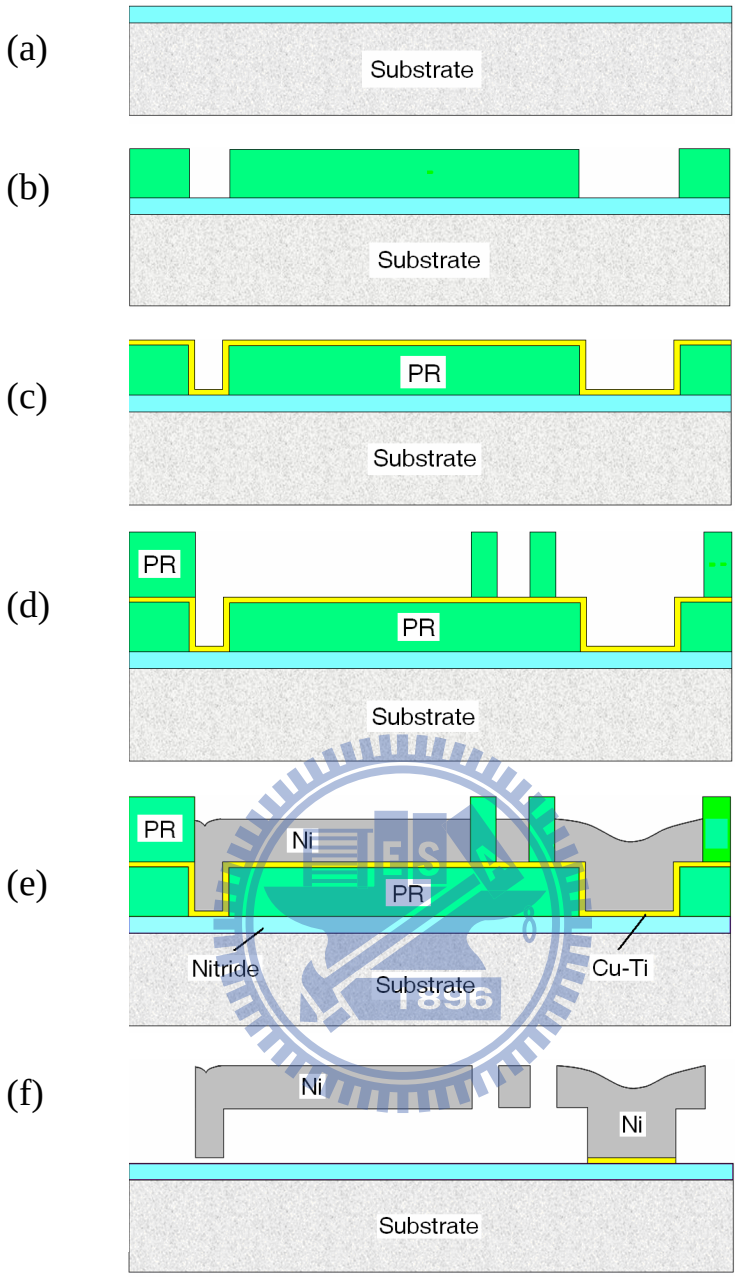

Figure 4-1. Fabrication process of micro-electroplated nickel SDA. (a) LPCVD Si_3N_4, (b) bushing and fixture patterning, (c) Cu/Ti seed layer, (d) device structure patterning, (e) nickel electroplating, (f) release.

Table 4-1. Lithography parameters

Photoresist	FH6400	AZ9260
Thickness	2.1 μm	5 μm
Spinning	500 rpm (10 sec) 1200 rpm (25 sec)	1000 rpm (10 sec) 5000 rpm (30 sec)
Waiting	5 min	10min
Soft Bake	2 min	10 min
Hydration	5 min	> 20 min
Exposure	3 sec (+20%) (46mW/cm^2)	6 sec (+20%) (46mW/cm^2)
Develop	30 sec (AZ-400k)	2 min 30 sec (AZ-400k)
Fix	1 min (DI Water)	1 min (DI Water)
Hard Bake	10 min	X

Table 4-2. Electroplating parameters

Mask	Mask #2
Metal	Nickel
Area	3.526 cm^2
Current Density	10 mA/cm^2
Electroplating Rate	0.2 μm/min

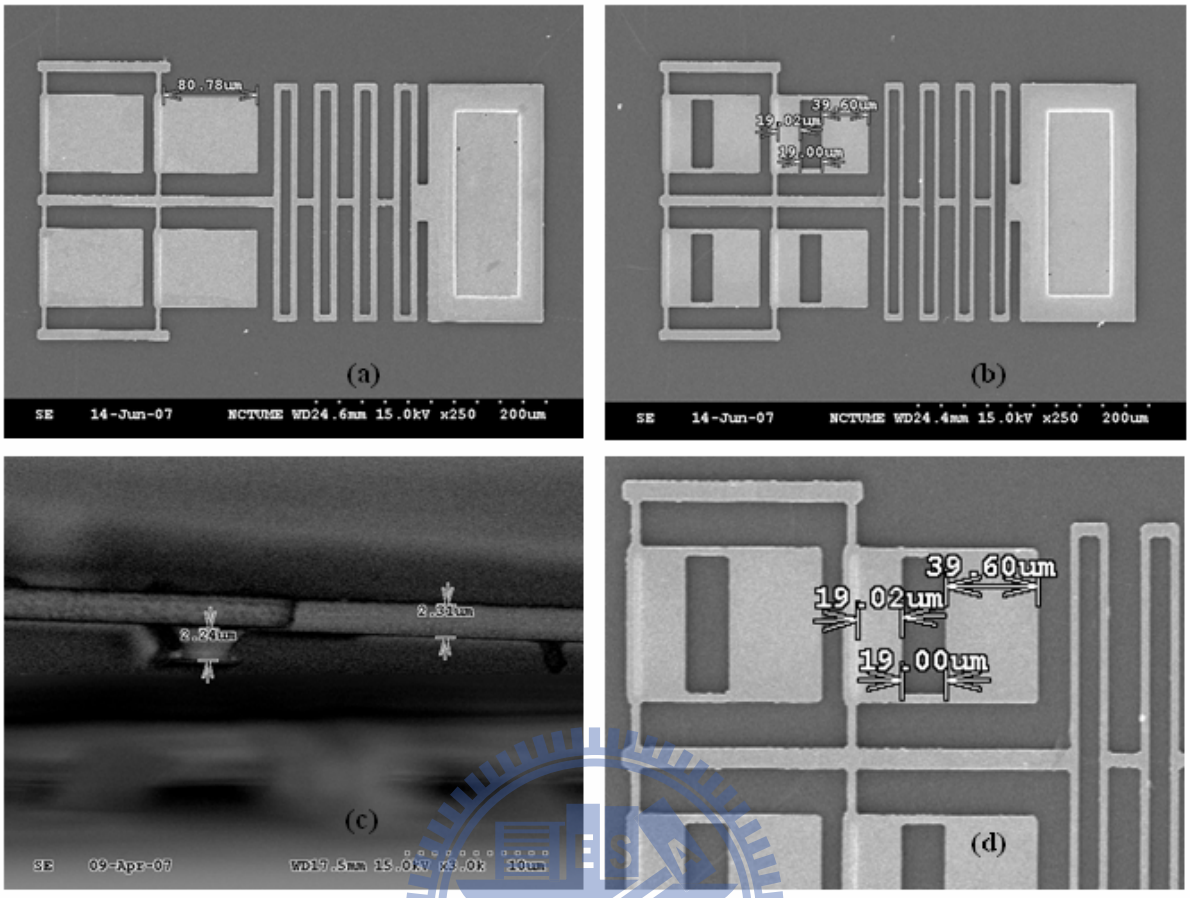

Figure 4-2. SEM pictures of fabricated results. (a) Top view of SDA array; (b) Top view of LVSDA array; (c) Side view of bushing and main plate; (d) Close up of LVSDA.

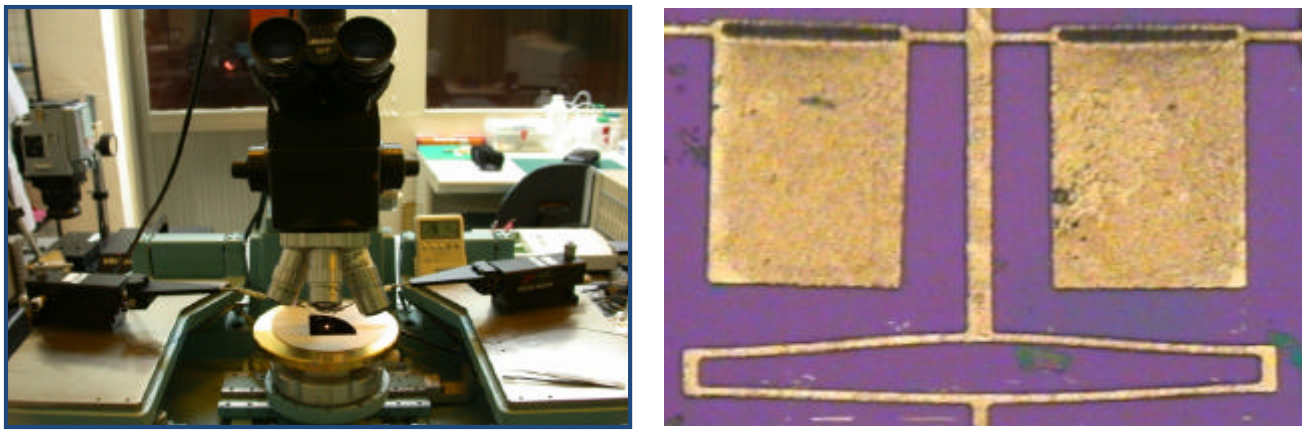

Figure 4-3. Driving test of released devices. (a) Measurement set-up, and (b) driving test of SDA array.

4.2 Analytical and testing results of SDA

In this subsection, the simulated and numerical results of SDA model developed in chapter 2 will be presented and compared with testing results of Ni SDA of 80 μm long and 65μm wide. Some discussions will be made on the key factors of SDA performance.

4.2.1 Static analytical results of SDA

Numerical codes on Matlab™ software are developed to perform the deflection analysis on the first proposed model based on parameters listed in Table 1. The non-contact length l_n is calculated first from Eq. (2-16) at each specified input voltage from 40 to 120 volts with increment in 10 volts. The results are plotted in Figure 4-4 where the non-contact length in this work is shorter than that of Kazuaki's work. As the simulation of electrostatic force in this work is better than Kazuaki's work, the chosen size of SDA may be smaller and save the chip size. The priming voltage V_{pr} of the device is calculated from Eq. (2-17) as shown in Figure 4-5. All models, including this work, Linderman's and Kazuaki's works, how that shorter plate needs higher priming voltage to maintain the contact between main plate and dielectrics. This work still shows smaller priming voltage than that of the other two models for same plate length. The step size for different control method out of Eq. (2-23) and Eq. (2-24) are plotted in Figure 4-6. The step sizes in fully-discharged mode of this work and Kazuaki's work have been shown in Figure 4-6(a). As the main plate tends to turn over at the end of discharge, the SDA operation is not stable enough. Consequently, constantly-contact mode is a stable way for SDA operation as shown in Figure 2-5. The SDA is driven between two input levels which are all equal to or larger than priming voltage, and the main plate always keeps contact with dielectrics during charge and discharge cycles. The step size in this mode is the step size at maximum input minus the step size at minimum input. Figure 4-6(b) shows the results when priming voltage is the minimum.

In Figure 4-7(a), the first reported bending moment diagrams of SDA are shown based on Eq. (2-20). The bending moment is zero over the entire contact part and at the starting point of non-contact part. Then it increases rapidly to maximum; after that, it goes down to the local minimum at the right end. The value of maximum moment and where it happens depends on the input level. From the trajectory of maximum moment M_m, it is obvious that M_m becomes higher and shifts rightward as input increases. The maximum static bending stress s_m along main plate for different input is plotted in Figure 4-7(b). This maximum stress, calculated by Eq. (2-21) as from 182 to 495 MPa for input voltages from 40 volts to 120 volts, also locates at same place of maximum moment for same input voltage.

Some mechanical properties of micro-fabricated Nickel useful in this work are adopted from literature; the Young's modulus of Nickel is chosen as 171 MPa; the yield strength is chosen as 323 MPa [32, 33]; the ultimate strength is chosen as 560 MPa [34, 38]. As the fatigue strength, [29] reported a value of 195 MPa for one million life cycles and constructed the S-N curve of Nickel under cyclic reverse loading test. For the driving test in continuously charge/discharge, the suitable failure mode is fatigue instead of yielding stress for static load. This topic will be discussed in subsection 4.2.2.

4.2.2 Dynamic analytical results of SDA

As some devices fail at higher voltage, it is proper to adopt the fatigue design theory [30] for cyclic loading to explore the cause. For a fully reversal loading with zero average stress, the stress amplitude s_R and the device life cycles N is related by the Basquin's equation,

$$\log A = \log s_R + B * \log N , \qquad (4\text{-}1)$$

where the coefficients A and B can be determined from the fatigue test data. For a non-fully reversal loading with stress amplitude s_r and average stress s_{av} not being zero, it is readily to decide the equivalent stress amplitude s_R by the Goodman's equation, $s_R = s_r + s_{av} s_e / s_{ult}$,

where s_R is viewed as the stress amplitude in a fully reversal loading with same life cycles as the original loading set (s_{av}, s_r). In Goodman's equation, s_e represents the fatigue strength (endurance limit) for a 10^6 device life cycles, while s_{ult} is the ultimate strength for only one life cycle. As this work does not focus on fatigue life but on performance of SDA, the coefficients A and B are determined by using the experimental data presented in [31], where s_{ult} =560MPa, s_e =195 MPa for micro-fabricated Nickel. By using the Basquin's equation mentioned above, it is easy to find out that A=560 and B=0.0750547. The stress amplitude s_r and the average stress s_{av} are both equal to s_{max} /2 because the minimum bending stress is zero for fully discharged manner. Figure 4-8(a) shows the S-N (stress-life cycles) curve based on Basquin's equation. During the loading test, some devices really failed as revealed in S-N curve qualitatively, although the exact cycles were not recorded. Figure 4-8(b) shows the theoretical upper bound and lower bound of the SDA life cycles. The regime between the upper and lower bounds presume the life cycles of SDA operated between the constantly-contact mode and fully discharge mode.

In order to verify the dynamic behavior, cyclic loading simulations conducted by Simulink™ are performed at different input voltages of 500 Hz for the simplified SDA model of SDOF mass-spring-damper system. The Simulink™ model and function blocks of the Eq. (2-25) are constructed as Figure 4-9. The function block named Coulomb and viscous friction models the discontinuity at zero and linear gain otherwise. The offset corresponds to the Coulomb friction and the gain corresponds to the viscous friction. As a result, this block is implemented as

$$y = sign(u) * (gain * abs(u) + offset) \qquad (4-2)$$

where *y* is the output of function block, *u* is the input of function block, gain and offset are block parameters. The normal force is calculated from electrostatic force between contact areas for

each input voltage. The gravity force is ignored. Since the viscous friction coefficient and Coulomb friction offset are not yet known exactly for the current device and previous literatures, various parameter sets are simulated to find out the most matched parameter set with experimental results.

From the standard test specimen in this batch process, the device total mass m is 5.66e-10 kg and the spring constant is 2.19 N/m. The undamped natural frequency w_n of the equivalent SDOF system is $(k/m)^{1/2}$ which is about 67000 Hz. Figure 4-10 shows displacement response curves of three viscous friction coefficients, respectively. The steady-state average displacement becomes bigger as the input voltage increases. This average is nearly same no matter the viscous friction varies for same input voltage. It is evident that the oscillation amplitude at steady-state is biggest as μ is close to zero, the oscillation amplitude decays as μ increases, which means friction dissipates a lot of energy. The nonlinearity in SDA motion mostly comes from the Coulomb friction. To quantify this effect, the Coulomb offset at zero should be determined first. Figure 4-11 shows displacement response curves for three offset values and other parameters are fixed. As the offset increases, the average at steady-state is lower down to show energy dissipation of Coulomb friction. For zero offset at zero velocity, the response is same as viscous damping of same friction coefficient. For low offset value, the response shows SDA displacing with less oscillating amplitude than that of zero offset case. For higher offset value, the response shows SDA is displacing in step-wise manner with less steady-state average and oscillating amplitude. Although the step-wise motion is a good feature for microactuator, it responds somewhat slowly and takes too much time to complete the motion. It is realized that the response is quite sensitive to the variation of Coulomb offset value. To operate SDA successfully, the properties of contact surfaces should be studied well.

As mentioned earlier, the Coulomb offset and viscous friction coefficient are both not

known exactly in the experiment. It is therefore to apply a matching process to identify the closest parameters with experiment results. As the nonlinear nature of SDA motion, it is preferred to find the matching set by matrix method. There are three major parameters: viscous friction, Coulomb friction and spring constant. By changing the value of each parameter in each set, the simulated results from Simulink™ are compared to experimental results. Finally, a well matched set is found of which the viscous friction coefficient is *c/m*=4e6, the Coulomb friction offset is *m/m*=15000 and the spring constant is 2.19 $\mu N/\mu m$. These parameters are substituted into the Simulink™ model of SDA and the simulation results are plotted in Figure 4-12.

4.2.3 Experimental results

To verify the dynamic behavior, cyclic loading tests are performed at different input signal of 500 Hz. This input is composed of a DC offset at 30 volts often and AC voltage depending on the control command. For example, when the driving signal needs to vary in the range of 30 to 120 volts, the chosen DC offset is 30 volts and AC amplitude is 90 volts in peak to peak definition. The experimental results are collected and compared with Simulink™ simulation results of our mass-spring-damper model of SDOF system or finite difference equation. In measurement practice, since the step size is in nanometer scale, it is hard to measure each step size directly. It is easier to measure a longer travel distance after a certain input pulses. However, the step size will decrease with the increasing spring force, and equation (2-23) only provides the step size prediction without external loading. Here two difference equations are proposed to calculate the step size in each input pulse and the total travel distance of SDA array with a restoring spring force after certain input pulses:

$$\Delta x(n) = \Delta x_0 * (F_o - \mathrm{k} * x(n-1)) / F_o, \qquad (4\text{-}3)$$

$$x(n) = x(n-1) + \Delta x(n). \qquad (4\text{-}4)$$

where the *Dx(n)* is the step size at the *n*-th input pulse, and Dx_0 is the step size without

considering external load, calculated from equation (2-23). The *x(n)* is the total travel distance of SDA array after *n* input pulses, k is the spring constant, and F_0 is the initial output force of SDA array, calculated from equation (2-22). The *x*(0) is set to zero. Qualitative speaking, the restoring force of spring is small at the beginning of the test and the step size is close to the calculated value without external load. As the spring deflection increases, the step size decreases with the increasing spring load. When the SDA array can no longer pull the spring, the step size becomes zero.

Figure 4-13 shows calculation and measurement results of the travel distance in 1500 input pulses at five different input voltages, from 80 volts to 120 volts. As expected, the SDA array moves rapidly at the beginning of motion. Then, the movement tends to slow down with the increasing spring force until SDA array can no longer pull the spring, i.e. in equilibrium state. The stable state will comes faster at low input voltages, because a lower driving voltage provides a smaller output force. For example, at 80 volts, the SDA array stops moving after around 750 input pulses, and at 120 volts, the stable state is reached around after 1400 input pulses. The maximum deviation between the measured and calculated results is around 10%. However, as the surface condition is not so even after release, the SDA motion is not as smooth as expect. Besides the travel distance data during the whole motion had not been saved, the intermediate data point to check the curvature shortening effect on step size is not enough. These data will be one of the major topics in follow-up research. Figure 4-14 shows the output force plot of measured and simulated, and from Eq. (2-22). As the simulated results of Eq. (2-22) and Eq. (2-26) are based on one SDA, the measured output force is given by one fourth of the output force of 4-SDA array. It is observed that the force from Eq. (2-22) is static in nature as the only load is electrostatic load. The measured force is different with respect to Eq. (2-22) in about +0.5 or - 2.3 μN in average. In general, this work provides the first and reliable model to predict the output force of SDA for given input.

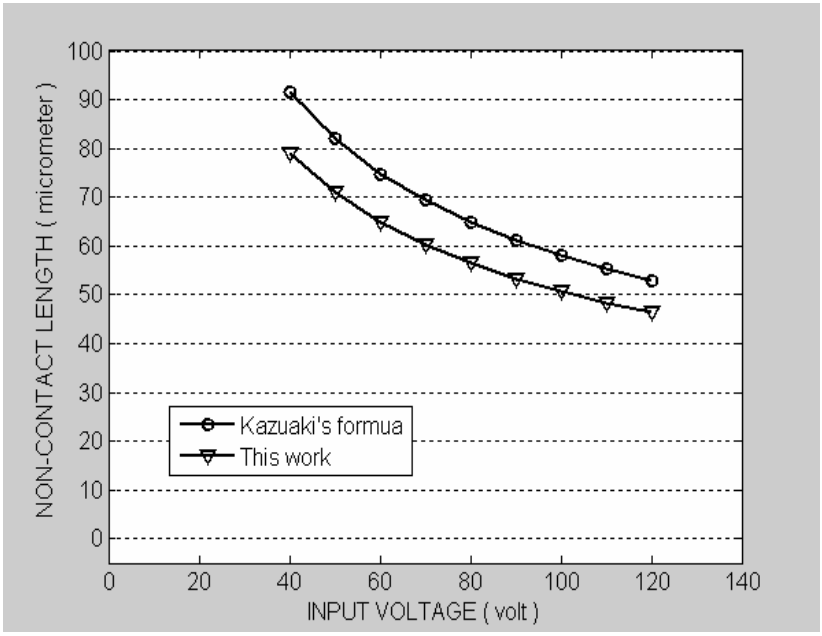

Figure 4-4. Non-contact length of SDA vs input voltage. Non-contact length means the minimum plate length to keep SDA priming for given input

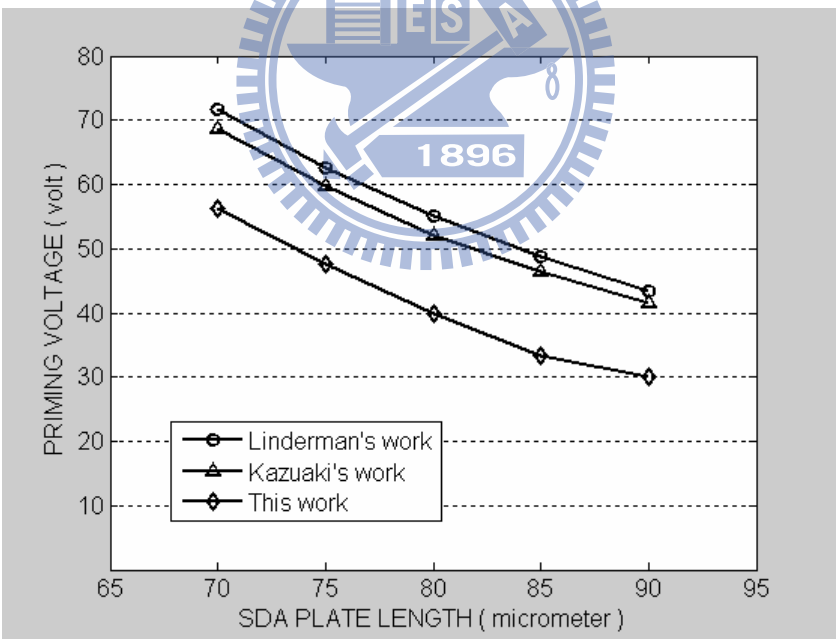

Figure 4-5. Simulated results on priming voltage. All models show shorter plate has higher priming voltage.

(a)

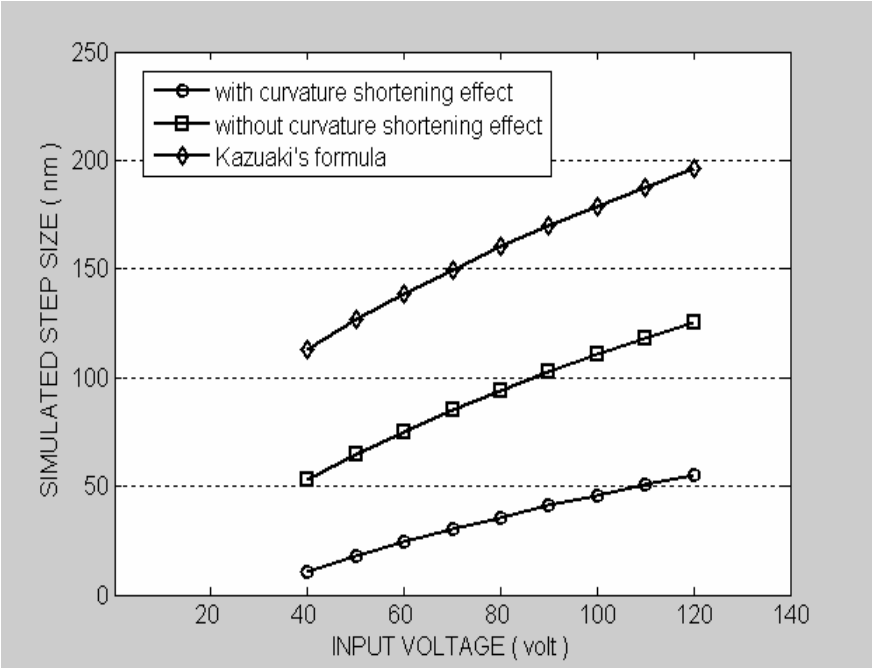

(b)

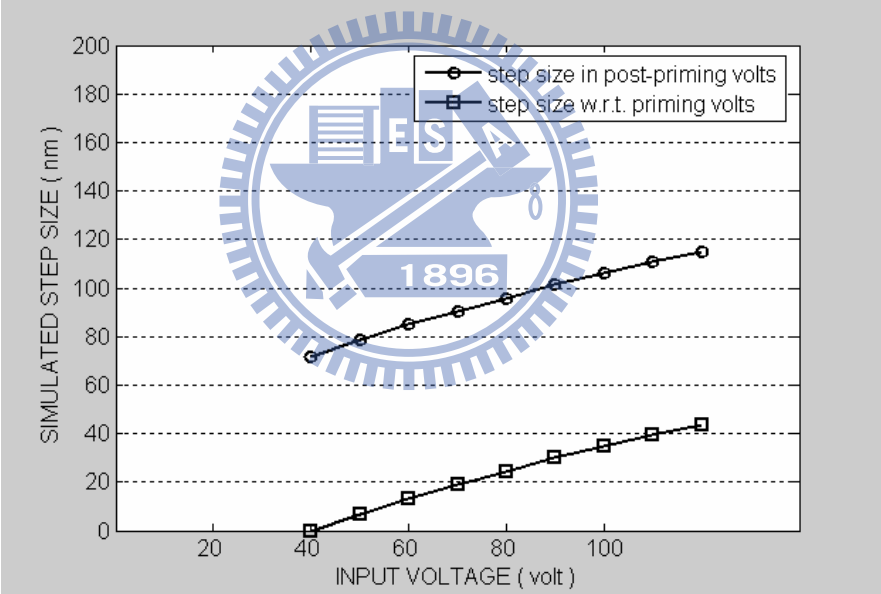

Figure 4-6. Simulated results on step size. (a) Step size for SDA operated in fully-discharge mode. (b) Step size for SDA operated in constantly-contact mode.

(a)

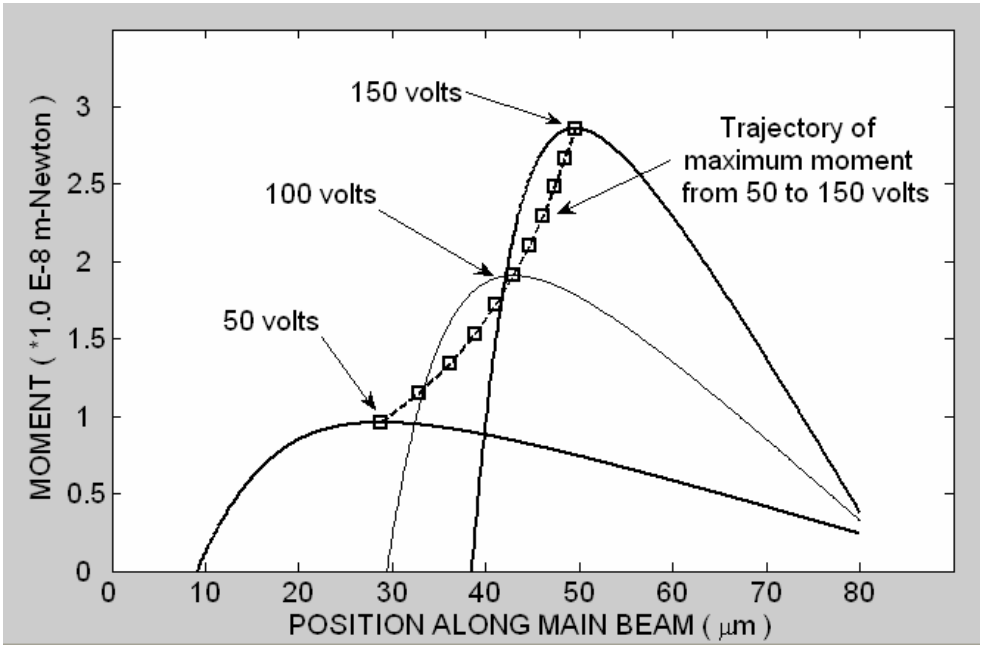

(b)

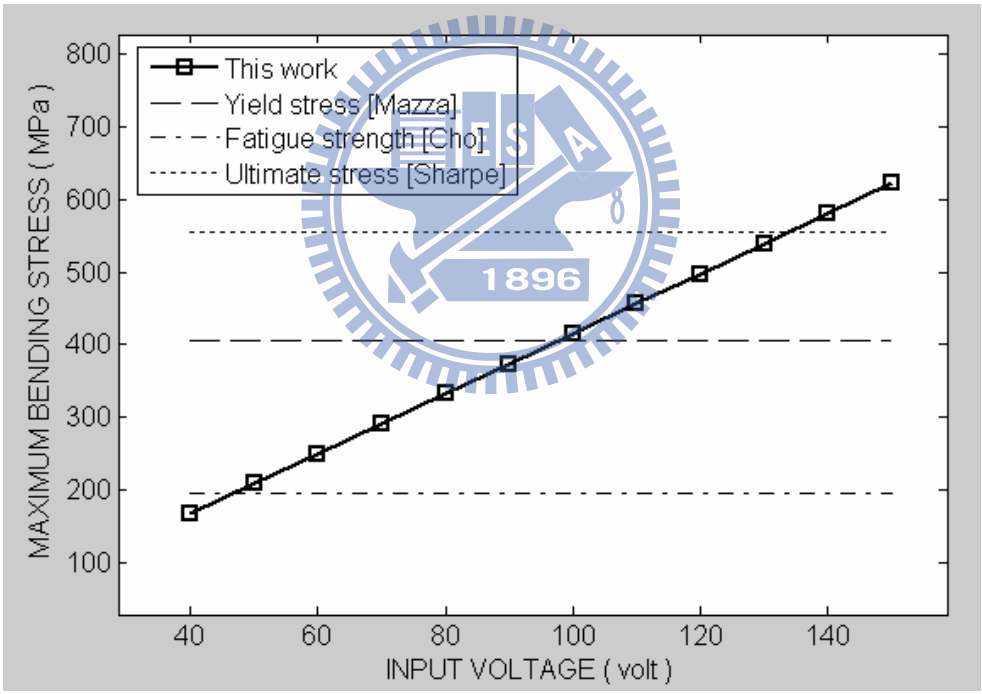

Figure 4-7. Simulated results on maximum bending moment and stress. (a) Bending moment diagrams along main beam for three levels of input voltage. The maximum moment M_m at each input is pointed by square symbol. Maximum moment M_m becomes higher as input voltage increases. (b) Simulated results on maximum bending stress in the definition of normal stress.

(a)

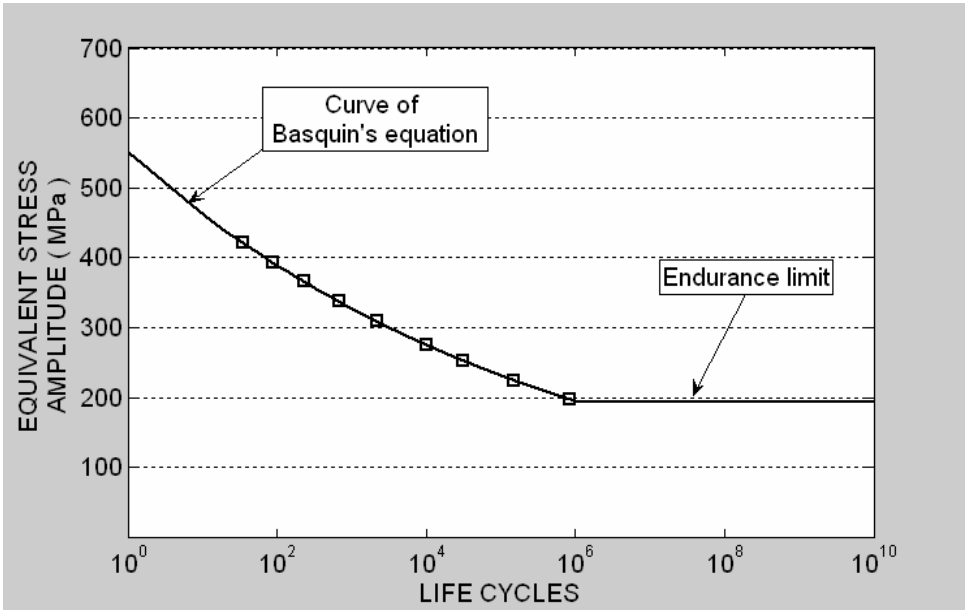

(b)

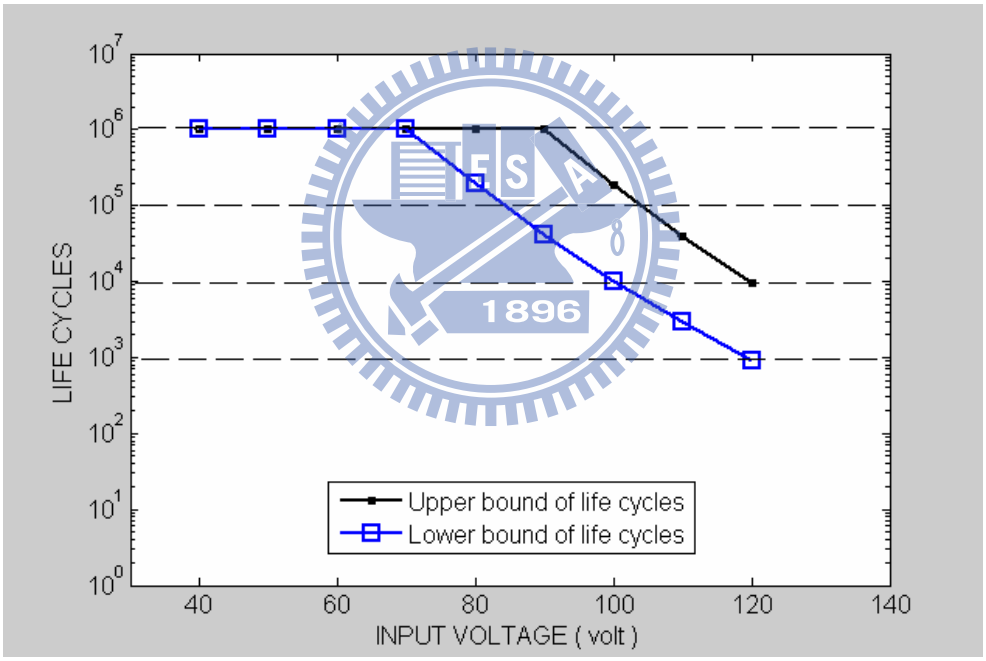

Figure 4-8. Fatigue behavior of Nickel SDA. (a) The S-N (stress against life cycles) curve of micro-fabricated nickel SDA array. (b) For given input, SDA life cycles are expected to be distributed between the upper and lower bounds of envelope.

(a)

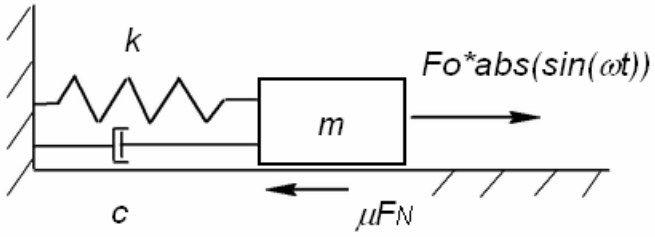

(b)

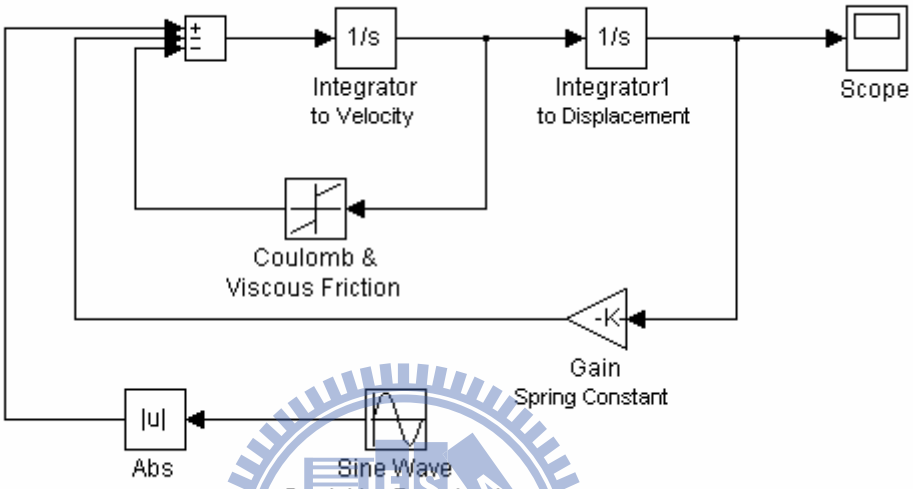

Figure 4-9. SDOF and Simulink Models of SDA. (a) dynamic system model of vibration induced motion, (b) the Simulink™ model of SDA array simplified as a mass-spring-damper system of SDOF.

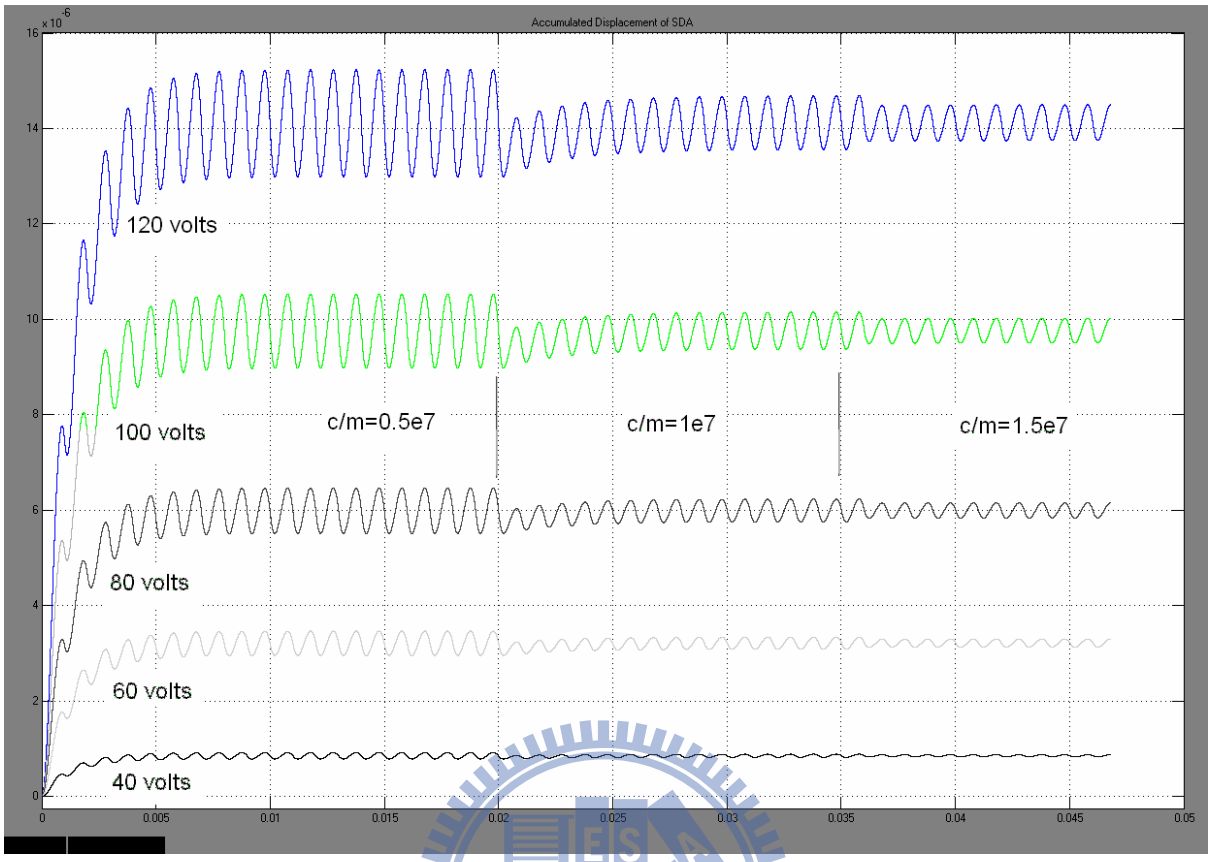

Figure. 4-10. Effects of viscous damping on displacement response. The average displacement at steady-state depends on driving input voltage, but oscillation amplitude at steady-state decreases at higher viscous friction. Parameters: 40, 60, 80, 100 and 120 volts driving at 3140rad/s, *c/m*= [0.5 1.0 1.5] *e7, *k/m*=3.8e9 and no Coulomb offset.

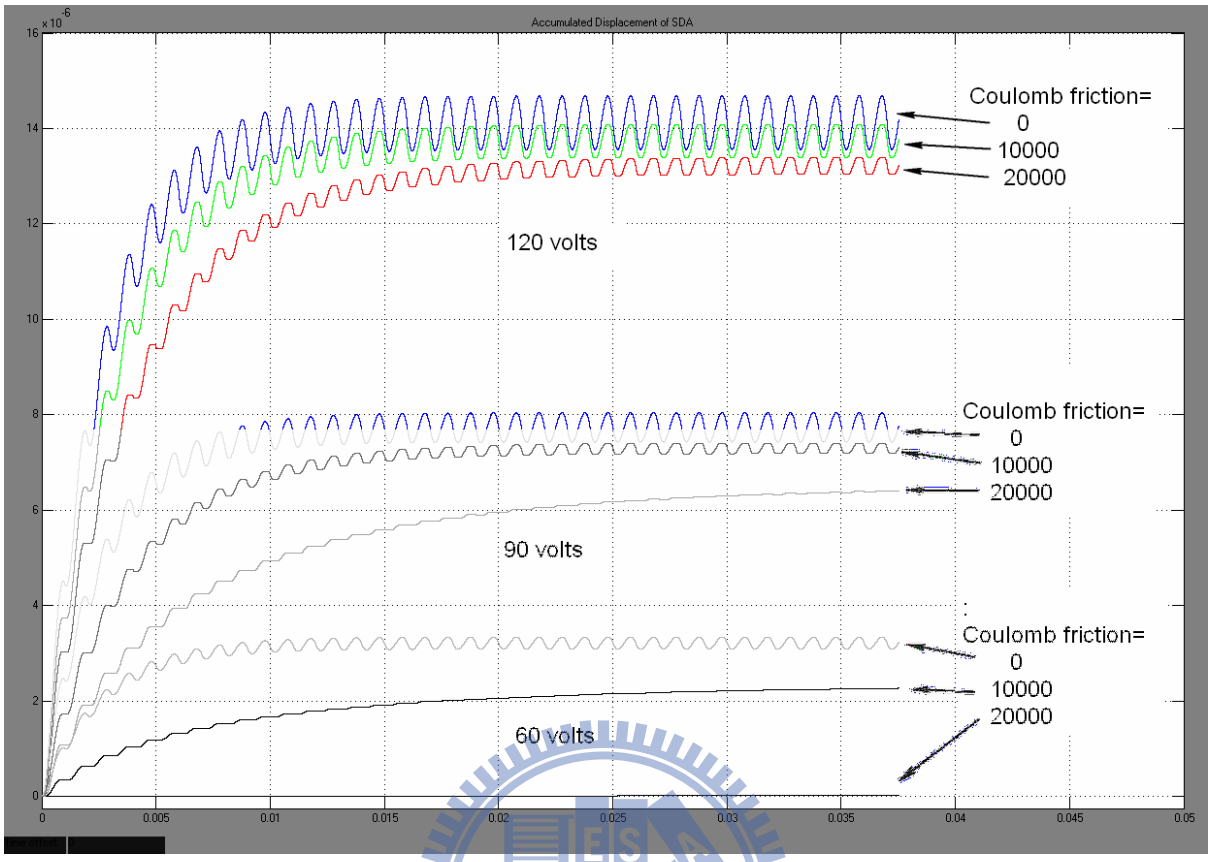

Figure.4-11. Effects of Coulomb offset on displacement response. The Coulomb friction will cause stick-slip motion and make the average displacement and oscillating amplitude at steady-state down to lower value. In the case of 60 volts, the motion even about stops. Parameters: 60 90 and 120 volts driing at 3140 (rad/sec), *k/m*=3.8e9, *c/m*=1.0e7, Coulomb offset= [0 10000 20000].

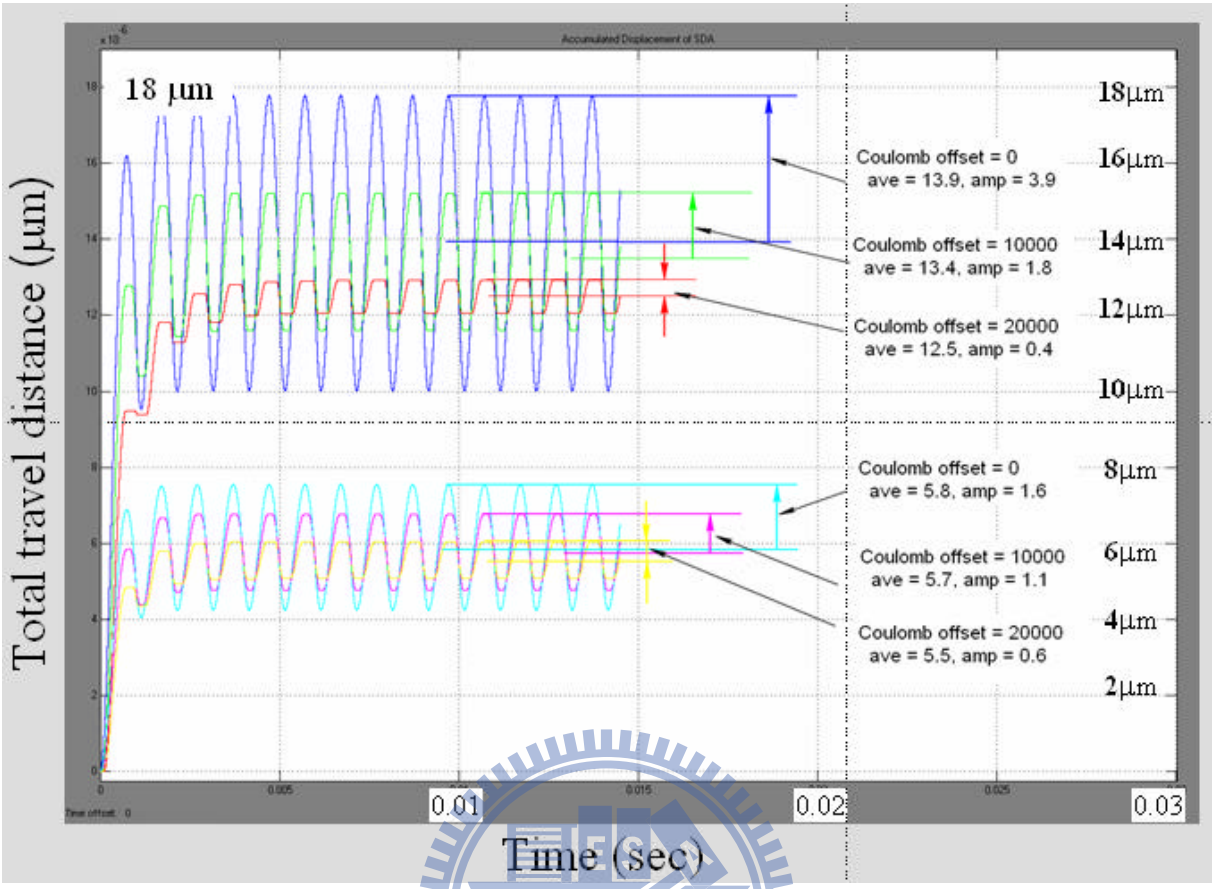

Figure 4-12. Matching the dynamical parameters by Simulink model. Parameters: 3140 (rad/sec), m=5.66e10 kg, k/m=3.8e9, c/m=4e6, Coulomb offset m/m= 15000.

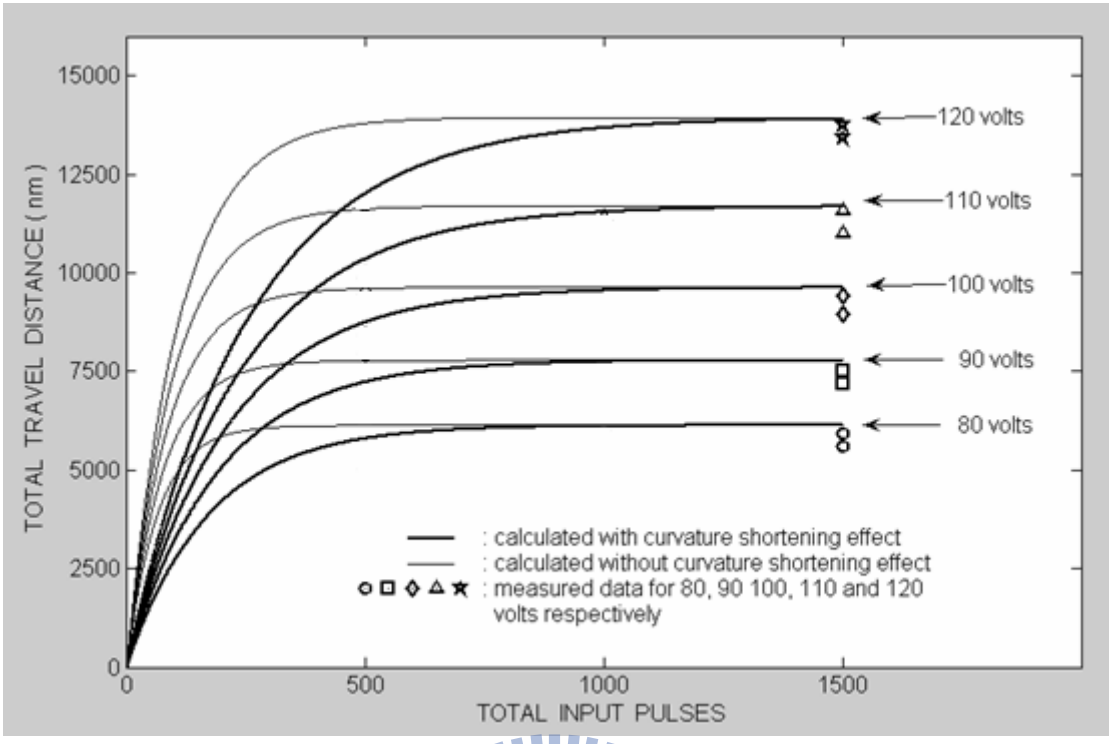

Figure 4-13. Measured and simulated total travel distances in 1500 input pulses for five different input voltages, from 80 volts to 120 volts. The SDA array moves rapidly at the beginning, then the movement tends to slow down with the increasing spring force until SDA array can no longer pull the spring, i.e. in equilibrium state. The simulated results are based on Eq. (4-3) and (4-4) by using step size with or without curvature shortening effect, respectively. As the total travel distance at steady-state depends on the ratio of input force to the spring constant in this finite difference formulation, the different step sizes will show their effects major in the traveling speed. This moving speed measurement during the motion, especially the first half time, will be executed in next batch of SDA fabrication and testing to verify the suitability of the proposed hypothesis of curvature shortening effect.

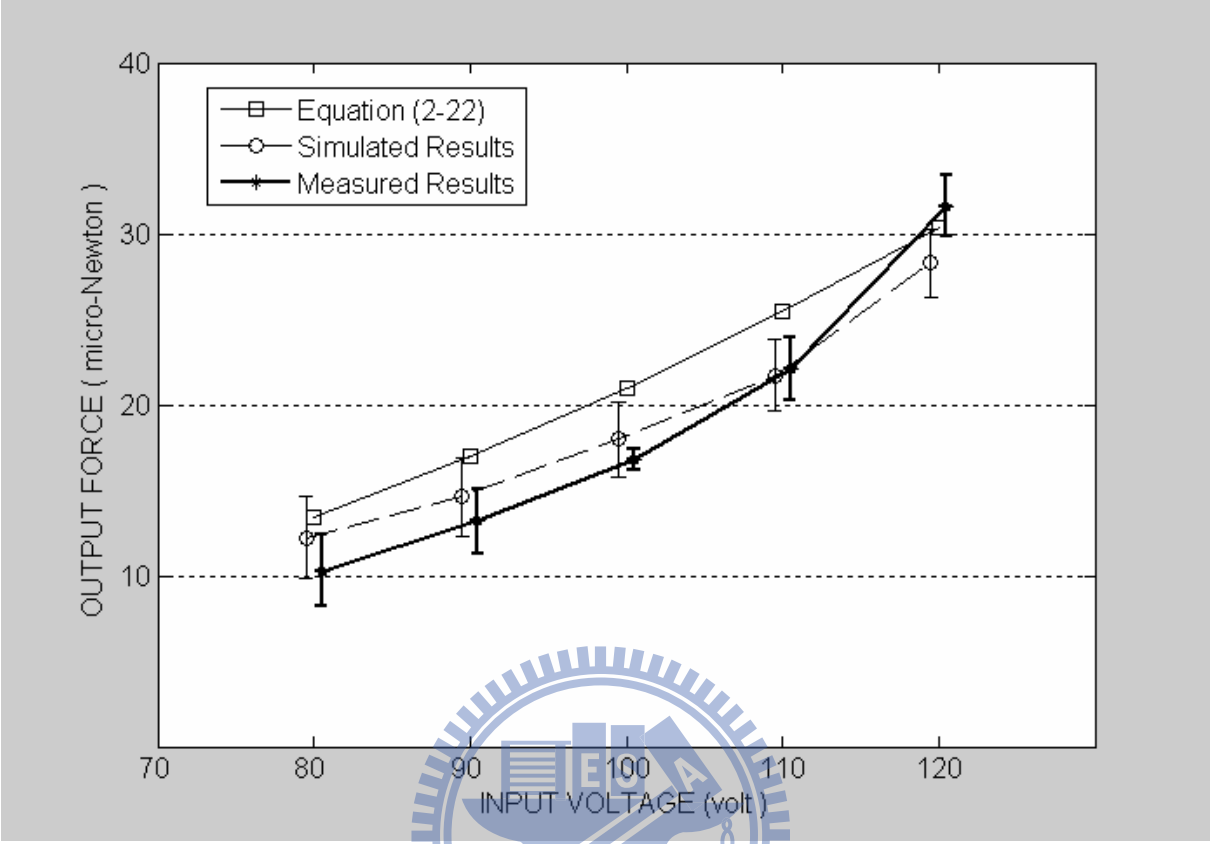

Figure 4-14. Output force plot of experimental and simulated results. Due to friction dissipates energy or induces stick-slip effect, the theoretical static output force is often higher than the measurement data. But sometimes the measured force exceeds the static output force due to the vibrational motion of SDA as data points shown at 120 volts.

4.3 FEA and testing results of LVSDA

Typical fabricated results earlier shown in Figure 4-2(a) and (b) show the top views of fabricated SDA array and LVSDA array, respectively. The measured main plate length of SDA is about 80.78 μm (Figure 4-2(a)), less than 1 μm deviation to the designed value of 80 μm. The bushing height and plate thickness for the device in Figure 4-2(c) are measured from SEM to be around 2.24 μm and 2.31 μm, respectively, a little larger than the designed value of 2.0 μm. From the close view of LVSDA shown in Figure 4-2(d), the measured scratch plate, flexible joint and main plate length of LVSDA are about 19.02 μm , 19.00 μm and 39.60 μm respectively. In comparison to the designed values of 20 μm, 20 μm and 40 μm, the deviation is within 1 μm.

The testing of LVSDA devices are performed at room temperature. The driving voltage is applied to contact electrode and substrate electrode through probes. The input signal is a cyclic wave of 500 Hz from the function generator with a high-voltage amplifier. The motion images are taken by a CCD camera mounted on the optical microscope and recorded in computer. This input is composed of a DC offset at 30 volts often and AC voltage depending on the control command. For example, when the driving signal needs to vary in the range of 30 to 120 volts, the chosen DC offset is 30 volts and AC amplitude is 90 volts in peak to peak definition. However, the LVSDA may not move until input voltage reaches certain threshold value. Output displacements are measured from the recorded images. The output force can be determined from the product of spring constant and total spring deflection at the corresponding input voltage.

In this section, the effects of geometric parameters on the performance of LVSDA will be presented and compared with conventional SDA. Simulation results from FEA will also be shown to discuss the effect of yielding stress to the maximum output force on the proposed

LVSDA. The device is at rest before threshold voltage in Figure 4-15(a). The threshold voltage is found to be around 46 volts. When driving voltage is 70 volts, as shown in Figure 4-15(b), the total tether spring deflection measured from image is 19.2 μm. The tether spring constant can be calculated as 1.98 μN/μm. The output force from four LVSDAs is then 1.98*19.2=38.1 μN. Therefore, output force of one such LVSDA can be determined to be about 9.53 μN at 70 volts. It is noted that there are at least three batch processes to fabricate the SDA and LVSDA array; the resultant dimensions show some deviations. The spring constant for LVSDA is about 1.98, and for SDA, the spring constant is about 2.19 μN/μm.

Figure 4-16(a) shows the measured output force trajectories of the conventional SDA and three types of LVSDAs with different scratch plate lengths L_s, 10μm, 15μm, and 20μm, respectively. All devices have the same total plate length of 80 μm and the same total plate width of 65 μm. All LVSDAs in Figure 30 have the same joint length L_j=20 μm and the same joint width W_j= 12 μm. Each data point is the average of at least five test results. It shows that the minimum required voltages, so-called threshold voltage, of all LVSDA are in the range from 40 volts to 50 volts, much lower than 80 volts which the conventional SDA needs at least to generate displacement. It verifies that the proposed LVSDA can reduce the threshold voltage effectively. LVSDA with a longer scratch plate a needs lower threshold voltage. As shown in Figure 4-16(a), threshold voltages for L_s= 20μm, 15μm, and 10μm are 40 volts, 46 volts, and 50 volts, respectively. A longer scratch plate represents the flexible joint is farther away from the bushing, so the flexural rigidity with respect to the main plate is smaller. Therefore, the mechanical force to overcome by electrostatic force is smaller for LVSDA with a longer scratch plate, i.e. a lower driving voltage is enough to activate the device.

However, output force of LVSDA reaches the maximum at certain driving voltage, and then starts to decline with the increasing input voltage as shown in Figure 4-16(a); unlike the output force of conventional SDA which keeps going up with the increasing input voltage. This can be

explained by the yielding effect. The maximum stress trajectories for devices with different scratch plate lengths analyzed by CosmosWorks® are plotted in Figure 4-16(b). In general, increasing input voltage will increase the output force in LVSDA or SDA before the yielding. Once the device yields, the output force would decline due to the reduced stiffness in plastic deformation. Therefore, the maximum output forces of different LVSDAs may not be the same and may occur at different input voltages. From Figure 4-16(b), LVSDA with longer scratch plate is easier to reach the yielding point, where the maximum output forces for L_s= 20 μm, 15 μm and 10 μm are 13.3 μN, 17.6 μN, 19.5 μN at 80, 100, and 110 volts, respectively (Figure 4-16(a)). It is also noted that, for example, LVSDA with flexible joint closer to the bushing (L_s=10 μm) can provide better performance than the output level of the conventional SDA up to 100 volts. Even at 110 volts, performance of LVSDA with L_s=10 μm is still close to the SDA.

The rigidity of flexible joint will be affected by joint length L_j, joint width W_j or thickness t. As the thickness is fixed in this work (2 μm), the effects of joint length and width are investigated here from the measured data and FEA results shown in Figure 4-17. A longer or narrower joint also means smaller flexural rigidity, which is helpful in reducing the threshold voltage. As shown in Figure 4-17(a), where scratch plate length L_s is fixed at 15 μm, the LVSDA with L_j=20 μm, W_j=6 μm has the lowest threshold voltage about 41 volts, comparing to other LVSDAs with shorter or wider flexible joints. For the same joint length, LVSDA with wider joint can output larger forces. For example, as shown in Figure 4-17(a), the maximum output force of device LV-15-20-45-12 (L_j=20 μm, W_j=12 μm) is 17.9 μN at 100 volts, larger than the maximum output force of device LV-15-20-45-6 (L_j=20 μm, W_j=6 μm) with 10.8 μN at 70 volts, since yielding stress for a wider joint happens at higher input voltage (Figure 4-17(b)).

Similar trend can be found in devices LV-15-15-50-12 (L_j=15 μm, W_j=12 μm, 19.6 μN at 110 volts) and LV-15-15-50-6 (L_j=15 μm , Wj=6 μm, 15.2 μN at 90 volts) in Figure 4-17(a). When the joint width increases, maximum stress in LVSDA would happen at higher voltage.

Figure 4-18 shows the simulated maximum stresses of device LV-15-15-50-W_j with different joint widths at various input voltages. It can be found that the maximum stress in LVSDA could be lower than yielding stress at 120 volts with W_j=25 or 45 μm. When the joint width increases, LVSDA in high-voltage region behaves more close to the conventional SDA. In another words, the conventional rectangular SDA can be considered as a special case of the proposed LVSDA where the joint width is equal to main plate width.

Longer flexible joint beam can also reduce the flexural rigidity. As shown in Figure 4-17(a), for devices LV-15-15-50-12 (Lj=15 μm) and LV-15-20-45-12 (Lj=20 μm), they both have the same scratch plate length and joint width, and the maximum force of device with the shorter flexible joint can provide a little larger maximum output force at higher input voltage (19.6 μN at 110 volts) than the device with longer joint (17.9 μN at 100 volts). It is a trade-off situation. Before yielding, using flexible joint can reduce the flexural rigidity, which is helpful in reducing the threshold voltage and provide a larger output force than SDA at the same input voltage. However, the achievable maximum output force will be limited due to the yielding effect in flexible joint. Consequently, by choosing the geometric parameters, such as joint width and location, LVSDA may operate in low-voltage region where the conventional SDA can not work, and still provide comparable performance as SDA in high-voltage region.

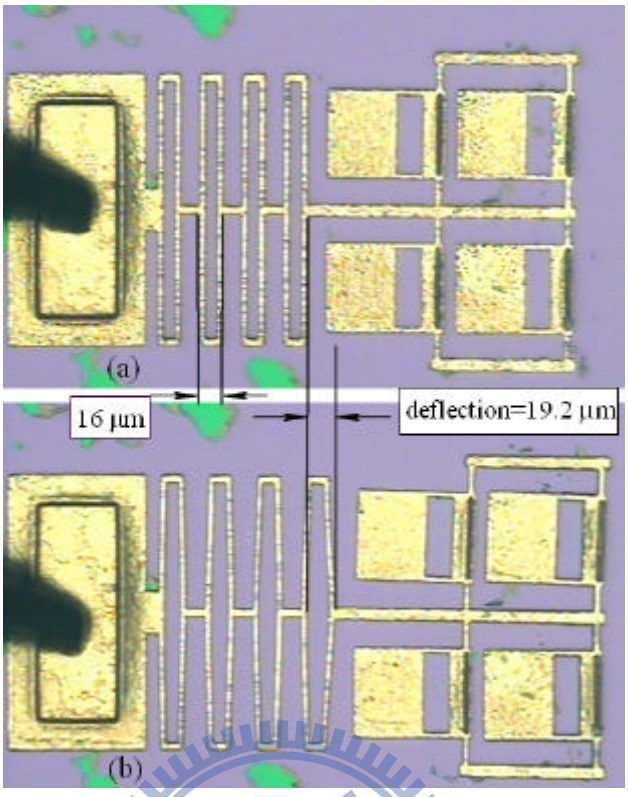

Figure 4-15. Driving test and measurement of device LV-10-20-50-6

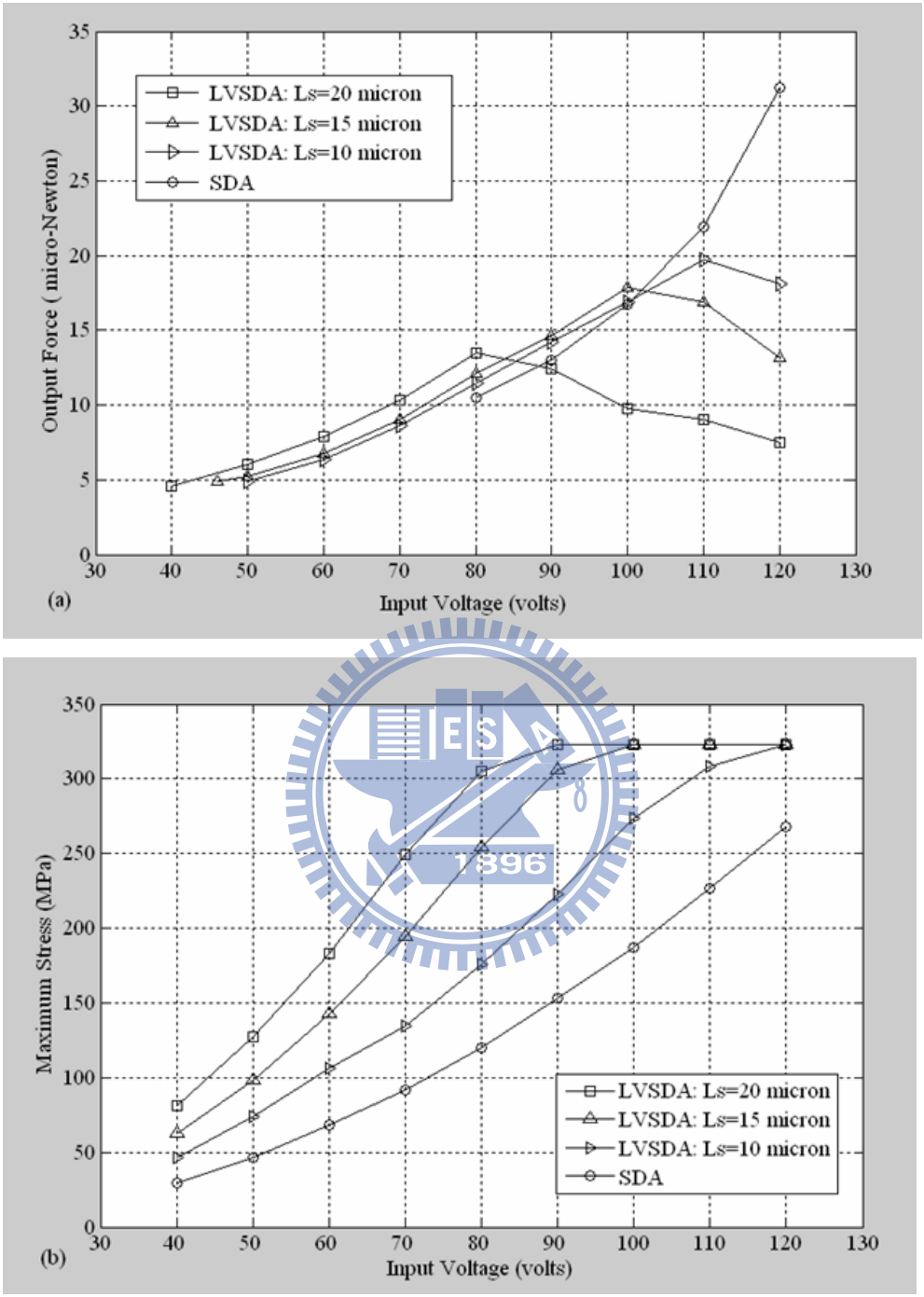

Figure 4-16. Effects of scratch plate length. (a) Measured output force trajectories of LVSDA and SDA; (b) Maximum stress of LVSDA and SDA by CosmosWorks®. All LVSDA devices have the same joint length 20 μm and joint width 12 μm. The sum of main plate length and scratch plate length is 60 μm.

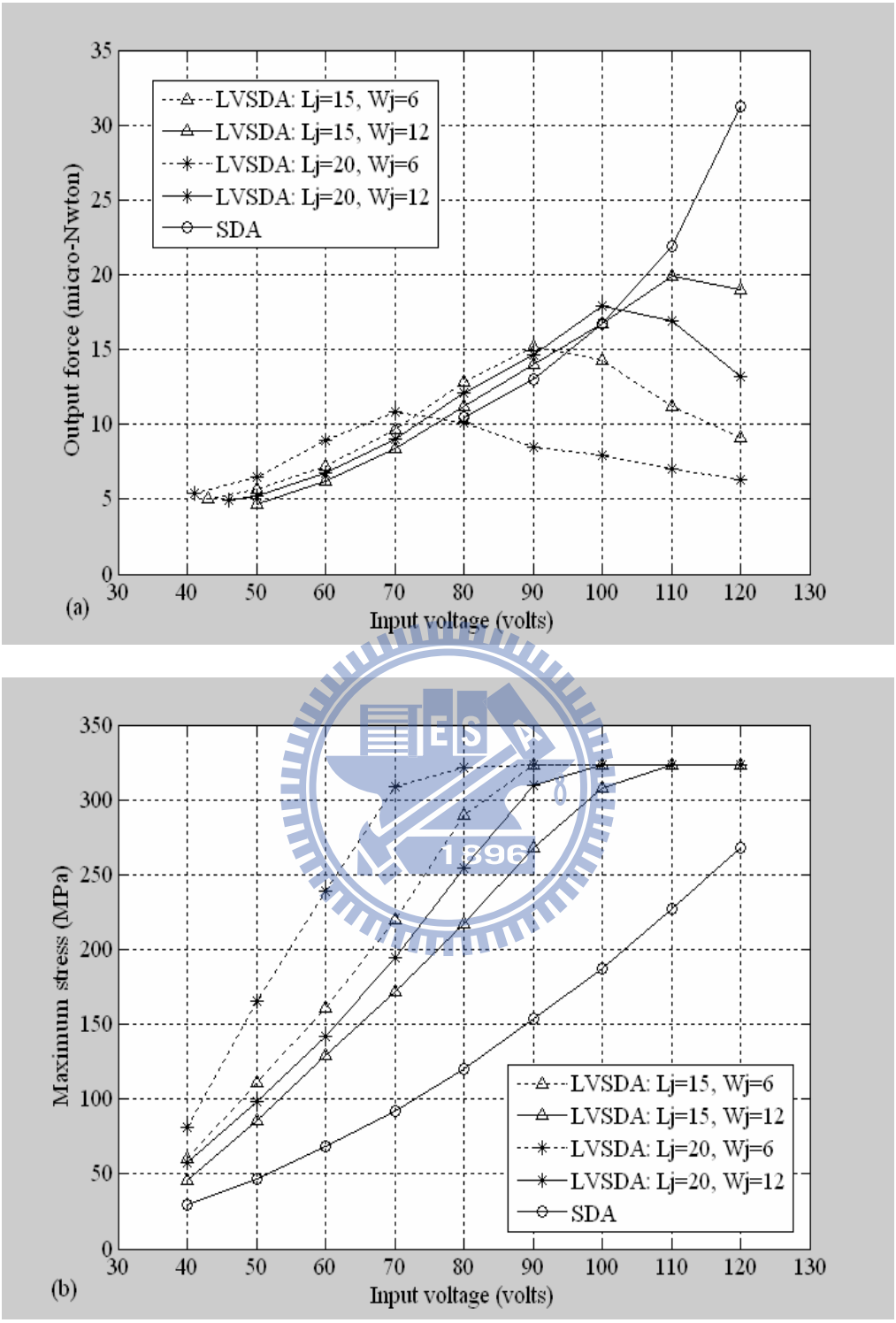

Figure 4-17. Effects of flexible joint width and length. (a) Measured output force trajectories of LVSDA and SDA. (b) Simulated maximum stresses of LVSDA and SDA by CosmosWorks®.

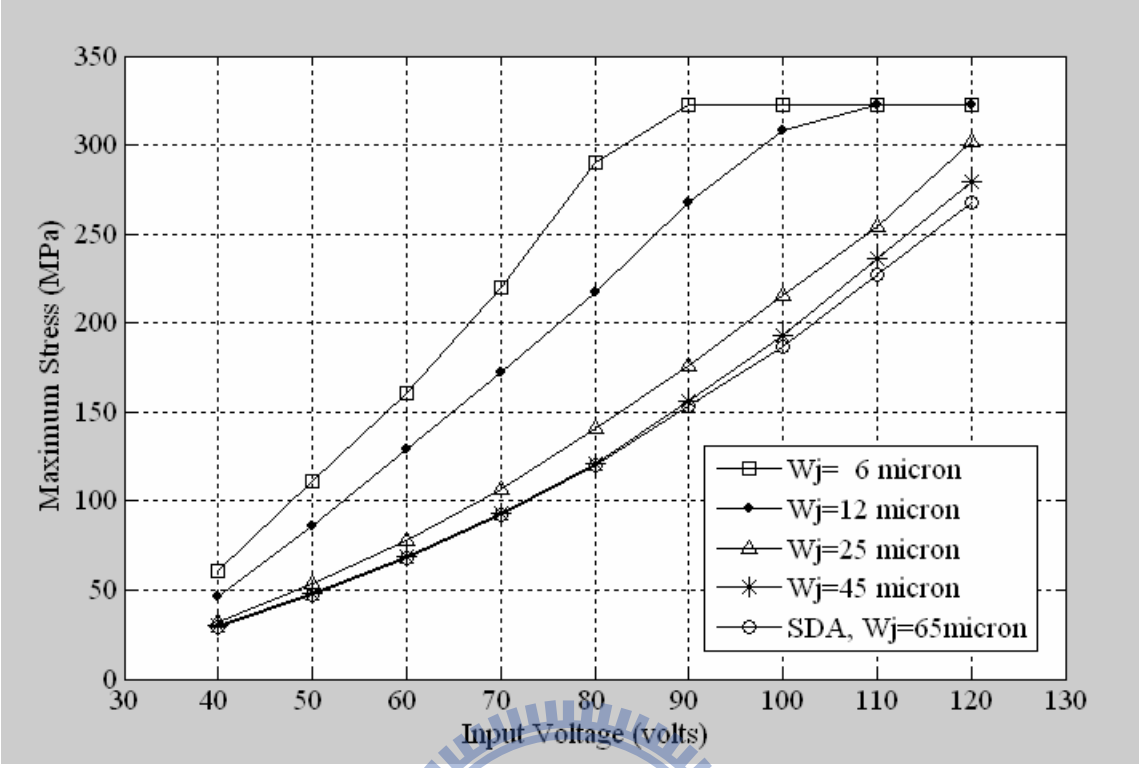

Figure 4-18. Simulated maximum stresses of device series LV-15-15-50-W_j at different input voltages

Chapter 5 Conclusions

5.1 Summary

Two analytical models, static and dynamic, of SDA have been proposed, simulated by Matlab™, Simulink™ and tested quite well with experiments. The first model performs static analysis of SDA and presents many key characteristics that were not presented all in previous literatures. The second model handles the SDA device as a mass-spring-damper system of SDOF to evaluate the dynamic properties. The vibration induced displacement of SDA subjected to various factors have been simulated and discussed in detail. A parameter set matched well with experimental results is suggested for the present micro-electroplated nickel SDA device to show the performance of output force and total travel distance for given cyclic input. In general, the analytical model proposed here may be modified to the design and analysis of SDA in other shape or made of any material. It is suggested that the proposed dynamic SDA model is suitable to analyze the stepwise behavior. However, it is not suitable to analyze the transient behavior due to lacking of the elastic-dynamic formulation at the beginning of contact which is beyond the scope of this work.

Another contribution here is to propose a low-voltage scratch drive actuator (LVSDA) to improve the SDA performance in low-voltage region by incorporating flexible joint into the conventional rectangular SDA. Experimental results show that at the same device size with total plate length of 80μm and width of 65μm, the threshold voltage can be reduced to locate in the range from 40 volts to 50 volts, evidently lower than 80 volts, the minimum required input voltage of the conventional rectangular SDA. A flexible joint longer, narrower, or further away from the bushing is helpful in reducing threshold voltage. It verifies that the proposed LVSDA

can be operated in low-voltage region where the conventional SDA can not. From the simulation results of FEA, it is found that yielding stress is a critical factor on output force. Before yielding, LVSDA can provide better performance than SDA at the same input voltage. However, it is a trade-off situation. Yielding is easier to happen in the flexible joint with smaller flexural rigidity in high-voltage region. Once yielding, output force will decline with the increasing voltage. The study shows that by varying the geometric parameters properly, such as joint width and location, LVSDA can still be operated in the low-voltage region where the conventional SDA can not and also provide comparable performance as conventional SDA in high-voltage region. The conventional rectangular SDA can be considered as a special case of the LVSDA where the joint width is equal to the main plate width. The proposed LVSDA may provide more flexibility in SDA design to meet different performance requirements, especially in the low-voltage region.

5.2 Future works

Though the SDA and LVSDA have been studied in analytical or experimental manners, and the simulated results can match the measured results in reasonable accuracy, there still have some works needed to improve the reliability and applicability of this research. The future works can be classified into five topics as following.

1. **Further experimental verification:**

Further experimental verification on dynamical response is quite necessary in general. For example, the non-contact length for given input is a lower bound of SDA main plate length, while a SDA with longer plate will still be priming with same non-contact length as implicated by Eq.(2-16). This argument somewhat violates with intuition but it is true. Evidence has been shown in [1], the contact length of three different main plates at same input level are recorded and plotted as shown in Figure 5-1. The contact length values for devices with plate length 60,

70 and 80 μm are 43, 53, and 63 μm respectively. In other words, the values of non-contact length are around 17 μm for these devices. This discovery supports the validity of this work's result. Why SDA of different plate length produces different force when the non-contact length is same? This problem can be probably simulated by introducing friction into the contact surface. An alternate method is applying the adhesion energy on contact part as done in [36], in which only the release problem is concerned. When taken adhesion effect into energy balance consideration, the adhesion will consume energy and reduce the mechanical displacement. These above discussions may be verified by fabrication and testing of next-generation design of SDA/LVSDA test structures.

2. Application on other SDA shapes:

Applied the analytical SDA model to plate shape beside rectangle is important in proving the model's applicability. This is basically routine but time-consuming work. The key point is the governing equation Eq. (2-2) is derived in general meaning, as it can be applied for other type of plate shape in case of the distributed load as Eq. (2-1) is expressed in suitable manner according to its shape as triangular, trapezoidal, or circular. Some previous works [37, 38] were done in pull-in research for these shapes under electrostatic force. Once the governing equation has been constructed, the steps followed are similar as presented in chapter 2 while the solution will be different. As the expressions are often complicated, this process may be somewhat tedious but the expected results will prove its great worth in predicting the device performance.

3. Reliability of SDA/LVSDA:

The load in SDA/LVSDA is basically dynamic. As a result, their life cycles rely on the material, loading/unloading level and geometric factors. To ensure the system be reliable in certain degree for guaranteed life cycles, the reliability design criteria should be introduced.

The S-N curve may be constructed after enough tested data have been collected and analyzed as derived in sections 2.3 and 4.2. Once the maximum and minimum stresses have been calculated from the input level, the expected life cycles can be decided from S-N curve. When the fatigue test data are enough, the endurance limit, yielding stress and ultimate stress of the fabricated devices can be determined from fatigue theory. These results may be utilized to improve the device design and process flow.

4. Analytical modeling of LVSDA:

Since the LVSDA is effective in reducing the threshold voltage than SDA of same width and length. It is worth of an analytical model, while it is more complicated in nature than SDA. The beam model proposed in Eq. (2-2) may be applied for LVSDA and the governing equations increase to three and are rather time-consuming to solve in analytical manner, though it is believed to be solvable. An alternative method is the application of pseudo-rigid-body model as Figure 5-2 for the main plate and scratch plate, while the flexible joint is still a beam. The main plate and scratch plate are viewed as rigid, while flexibe joint is still a beam. The minimum potential energy principle of the sum of elastic deformation energy and electrostatic energy in capacitor will decide the equilibrium generalized coordinates (θ_1, θ_2) at given input. This approach seems easier to derivate an analytical solution. Once the generalized coordinates (θ_1, θ_2) are determined, the other characteristics can be calculated by routine manner.

5. Optimization design of SDA/LVSDA:

The optimization of SDA/LVSDA on geometrical factors may be handled in two ways. The first one is the present method, i.e., by fabricating different devices and then testing for optimal geometrical set. For example, for a flexible joint with fixed length and width, the joint location will affect the output force level. The test results will reveal the optimal geometrical set of LVSDA. This approach is effective but expensive. Another one is to form the object function

with suitable constrain conditions by using the results in last topic: Analytical modeling of LVSDA and SDA modeling. These object function and constraint may be used in commercial software as Optimization Toolbox in MATLAB™.

6. Latch mechanism for stable step size:

Though the friction effect is the major operation principle of SDA/LVSDA, it also introduce instable step size. To minimize this defect, a rachet mechanism is proposed to fabricated along the trajectory of motion to fix the step size in mechanical manner. However, this design will confine the step size in the pitch of rachet teeth.

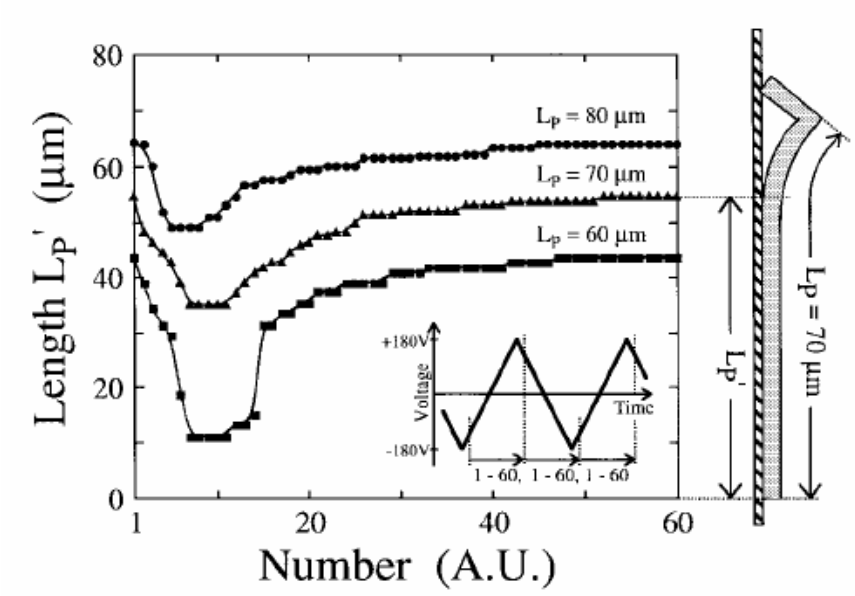

Figure 5-1. Contact and Non-contact length for different plate length [1].

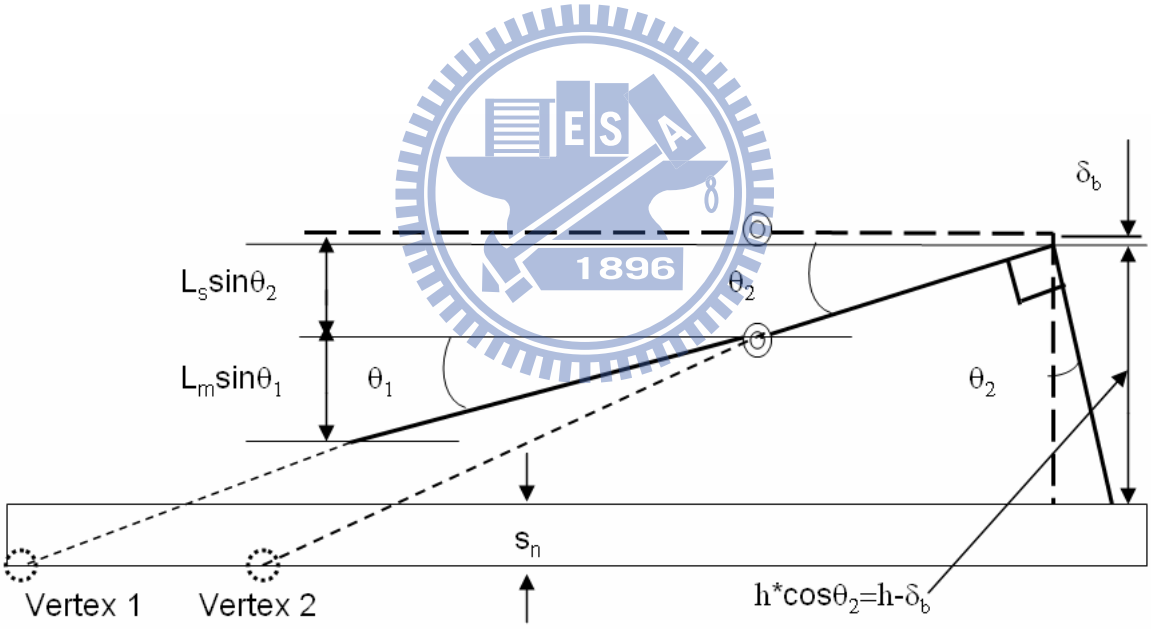

Figure 5-2. Pseudo-rigid-body model of LVSDA to find the equilibrium state of generalized coordinates (θ_1, θ_2) at given input level. The main plate and scratch plate are viewed as rigid, while flexibe joint is still a beam. The minimum potential energy principle of the sum of elastic deformation energy and electrostatic energy in capacitor will decide the equilibrium generalized coordinates (θ_1, θ_2) at given input.

References:

[1] T. Akiyama, D. Collard, and H. Fujita, “Scratch Drive Actuator with Mechanical Links for Self-Assembly of Three-Dimensional MEMS,” *J. Microelectromech. Syst.*, vol. 6, no. 1, pp. 10-17, 1997.

[2] T. Akiyama, and K. Shono, “Controlled Stepwise Motion in Polysilicon Microstructures,” *J. Microelectromech. Syst.*, vol. 2, no. 3, pp. 106-110, 1993.

[3] J. Zhu, T. Akiyama, and K. Shono, “A Micro Step Motion of Polysilicon Structures on Silicon Substrate,” *IEEE Japan Int’l Electronics Manufacturing Technology Symposium,* Kanazawa, Japan, pp. 85-88, 1993.

[4] Y. Fukuta, D. Collard, T. Akiyama, E. H. Yang, and H. Fujita, ”Microactuated Self-assembling of 3D Polysilicon Structures with Reshaping Technology,” *TRANSDUCERS’97*, Chicago, IL, vol. 1, pp. 665-668, 1997.

[5] L. Fan, M. C. Wu, K. Choquette and, M. H. Crawford, “Self-Assembled Micro-XYZ Stages for Optical Scanning and Alignment,” *TRANSDUCERS’97,* Chicago, IL, vol. 1, pp. 319-322, 1997.

[6] C. K. Lee, Y. J. Lai, C. Y. Wu, J. A. Yeh and R. S. Huang, “Feasibility study of self-assembly mechanism for variable optical attenuator,” *J. Micromechanics and Microengineering*, vol.15, no.1, pp. 55-62, 2005.

[7] E. Quévy, L. Buchaillot, and D. Collard, “3-D Self-Assembling and Actuation of Electrostatic Microstructures,” *IEEE Transactions on Electron Devices,* vol. 48, no. 8, pp. 1833-1839, 2001.

[8] R. J. Linderman, and V. M. Bright, “Nanometer Precision Positioning Robots Utilizing Optimized Scratch Drive Actuators,” *Sensors and Actuators*: A 90, no. 3, pp. 292-300, 2001.

[9] Y. Kanamori, Y. Aoki, M. Sasaki, H. Hosoya, A. Wada, and K. Hane, “Fiber-optical switch using cam-micromotor driven by scratch drive actuators,” *J. Micromech. Microeng.*, vol. 15, pp. 118–123, 2005.

[10] R. J. Linderman, P. E. Kladitis, and V. M. Bright, “Development of micro rotary fan,” *Sensors and Actuators*: A 95, no. 2, pp.135–142, 2002.

[11] P. E. Kladitis, R. J. Linderman, and V. M. Bright,” Self-assembled Micro Axial Fan Driven by a Scratch Drive Actuator Rotary Motor,” *IEEE MEMS*, Interlaken, Switzerland, pp. 598-601, 2001.

[12] B. R. Donald, C. G. Levey, C. D. McGray, D. Rus, and M. Sinclair, “Power Delivery and Locomotion of Untethered Microactuators,” *J. Microelectromech. Syst.*, vol. 12, no. 6, pp. 947-959, 2003.

[13] B. R. Donald, C. G. Levey, and I. Paprotny,” Planar microassembly by parallel actuation of MEMS microrobots,” *Journal of Microelectromechanical Systems*, vol. 17, no. 4, pp. 789-808, 2008.

[14] B.R. Donald, C. G. Levey, C.D. McGray, D. Rus, and M. Sinclair, “Power Delivery and Locomotion of Untethered Microactuators,” *IEEE MEMS*,Kyoto, Japan, pp. 124-129, 2003.

[15] E. Dumsong, N. Afzulpurkar, and A. Tuantranont, “Design, Analytical Modeling, and Simulation of Wire-free Walking Scratch-Drive Microrobt,” *IEEE Transactions on Industrial Electronics*, vol. 56, no. 4, pp. 1109-1119, 2009.

[16] O. Millet, P. Bernardoni, S. Regnier, P. Bidaud, E. Tsitsiris, D. Collard, and L. Buchaillot, “Electrostatic actuated micro-gripper using an amplification mechanism,” *Sensors and Actuators*, A 114, no. 3, pp. 371-378, 2004.

[17] Y. Kanamori, H. Yahagi, and K. Hane, “A microtranslation table with scratch drive actuators fabricated from silicon-on-insulator wafer,“ *Sensors and Actuators*, A 125, no. 2, pp. 451-457, 2006.

[18] Y. Mita, T. Oba, G. Hashiguchi, M. Mita, P. Minotti and H. Fujita, “An Inverted Scratch-Drive-Actuators Array for Large Area Actuation of External Objects,” *Transducers’99*, Sendai, Japan, pp. 1196-1197, 1999.

[19] C. P. Langlet, T. Akiyama, and H. Fujita, “Quantitative analysis of scratch drive actuation for integrated X/Y motion system,” *Proceedings of the International Conference on Solid-State Sensors and Actuators’* , Tokyo, Japan, vol. 2 , pp. 773-776, 1997.

[20] H. Kazuaki, A. Torii, and A. Ueda, “An Analysis of the Elastic Deformation of an Electrostatic Microactuator,” *Transaction of IEE Japan*, 118-E, no. 3, pp. 205-211, 1998.

[21] J. W. Zu, Q. Qu, and G. Cheng, “Analytical Modeling and Quantitative Analysis of Scratch Drive Actuator,” *Int’l Conference of MEMS, NANO and Smart Systems*, Alberta, Canada, pp. 629-635, 2004.

[22] L. Li, J. G. Brown, and D. Uttamchandani, “Comparison of theoretical and experimental determination of the flexing of scratch drive plates,” *Proceedings of the SPIE*, vol. 4928, Shanghai, pp. 180–189, 2002.

[23] L. Li, J. G. Brown, and D. Uttamchandani, ”Study of scratch drive actuator force characteristics,” *J. Micromech. Microeng.*, vol. 12, no. 6, pp. 736–741, 2002.

[24] Q. Qu, J. W. Zu, and G. Cheng, “Adhesion-related failure models for scratch drive actuators,” *J. Micromech. Microeng.*, vol. 14, no. 10, pp. 1405–1410, 2004.

[25] S. Timoshenko, and J. N. Goodier, *Theory of Elasticity*, (PA, MAPLE PRESS), 1951.

[26] A. Fidlin, *Nonlinear Oscillations in Mechanical Engineering*, (Berlin: Springer-Verlag),

2006.

[27] A. Fidlin and J. J. Thomsen, “Predicting vibration-induced displacement for a resonant friction slider,” *European Journal of Mechanics of Solids*, vol. 20, no. 1, pp. 155–166, 2001.

[28] J. J. Thomsen, “Some General Effects of Strong High-Frequency Excitation: Stiffening, Biasing and Smoothening,” *Journal of Sound and Vibration*, vol. 253, no. 4, pp. 807-831, 2002.

[29] N. Hinrichs, M. Oestreich, and K. Popp, “On the modelling of friction oscillators,” *Journal of Sound and Vibration(AP)*, vol. 216, no. 3, pp. 435-459, 1998.

[30] J. J. Thomsen, and A. Fidlin, “Analytical approximation for stick-slip vibration amplitudes,” *International Journal of Non-Linear Mechanics*, vol. 38, no. 3, pp. 389-403, 2003.

[31] M. F. Spotts, *Design of Machine Elements* (New Jersey: Prentice-Hall), 1985.

[32] W. N. Jr, Sharpe, D. Lavan, and R. Edwards,” Mechanical properties of LIGA deposited nickel for MEMS,” *TRANSDUCERS’97*, Chicago, IL, pp. 607-611, 1997.

[33] E. Mazza, S. Abel, and J. Dual,”Experimental determination of mechanical properties of Ni and Ni-Fe microbars,” *Microsyst. Technol.*, vol. 2, no. 4, pp. 197–202, 1996.

[34] L. S. Stephens, K. W. Kelly, S. Simhadri, A. B. McCandless, and E. I. Meletis,” Mechanical property evaluation and failure analysis of cantilevered LIGA nickel microposts,” *J. Microelectromech. Syst.*, vol. 10, no. 3, pp. 347-359, 2001.

[35] H. S. Cho, K. J. Hemker, K. Lian, J. Goettert, and G. Dirras, “Measured mechanical properties of LIGA Ni structures,” *Sensors and Actuators*: A 103**,** no. 1-2, pp. 59-63, 2003.

[36] Q. Qu, J. W. Zu, and G. Cheng, “Adhesion-related failure models for scratch drive actuators,” *J. Micromech. Microeng.*, vol. 14, no. 10, pp. 1405–1410, 2004.

[37] Y. Nemirovsky, and O. Bochobza-Degani, “A methodology and model for the pull-in parameters of electrostatic actuators,” *Journal of Microelectromechanical Systems*, vol. 10, no. 4, pp. 601-615, 2001.

[38] C. G. Agudelo, M. Packirisamy, G. Zhu, and L. Saydy, “Nonlinear Control of an Electrostatic Micromirror Beyond Pull-In with Experimental Validation,” *Journal of Microelectromechanical Systems*, vol. 18, no. 4, pp. 914-923, 2009.

Publication List

- Journal papers:
  - Shawn Chen, Chiawei Chang and Wensyang Hsu, "Output Force Enhancement of Scratch Drive Actuator in Low-Voltage Region by Using Flexible Joint," *Sensors and Transducers Journal*, Vol. 115, Issue 4, April 2010, pp.71-82.
  - Shawn Chen, Chiawei Chang and Wensyang Hsu, "Improved Model of Rectangular Scratch Drive Actuator," *Journal of Micro/Nanolithography, MEMS, and MOEMS*, (submitted).
  - Shawn Chen, Chiawei Chang and Wensyang Hsu, "Design, Fabrication and Testing of a Novel Low Voltage-driving Scratch Drive Actuator with Flexible Joint," *Sensors and Actuators: A*, (submitted).

- Conference papers:
  - Shawn Chen, Chiawei Chang and Wensyang Hsu, "Output Force Characterization of Scratch Drive Actuators with Flexible Joints", *APCOT*, Perth, Australia, July 6-9, 2010.
  - Shawn Chen and Wensyang Hsu, "Feasibility study on a novel low-voltage-driven fixed-step-size scratch drive actuator with flexible joint", *EUROSENSORS*, Barcelona, Spain, Sep. 11-14, 2005.
  - Shawn Chen and Wensyang Hsu, "Reversible stepwise motion by a novel symmetric scratch drive actuator", *ASME IMECE*, New Orleans, USA, Nov. 17-22, 2002.

簡歷(Vita)

學歷：國立交通大學工學博士(民國99年)

國立中央大學工學碩士(民國77年)

國立交通大學工學學士(民國71年)

經歷：國立勤益科技大學講師

國立勤益技術學院講師

私立勤益技術學院講師

研究方向：微致動器最佳化設計

創意性機構設計

油壓機械設計